

# The Sunyaev–Zel’dovich angular power spectrum as a probe of cosmological parameters

E. Komatsu<sup>1\*</sup> and U. Seljak<sup>2†</sup>

<sup>1</sup>*Department of Astrophysical Sciences, Princeton University, Princeton, NJ 08544, USA*

<sup>2</sup>*Department of Physics, Princeton University, Princeton, NJ 08544, USA*

31 May 2018

## ABSTRACT

The angular power spectrum of the Sunyaev–Zel’dovich (SZ) effect is a powerful probe of cosmology. It is easier to detect than individual clusters in the field, is insensitive to observational selection effects and does not require a calibration between cluster mass and flux, reducing the systematic errors which dominate the cluster-counting constraints. It receives a dominant contribution from virialized cluster region between 20 – 40% of the virial radius and is thus relatively insensitive to the poorly known gas physics in the cluster centre, such as cooling or (pre)heating. In this paper we derive a refined analytic prediction for the SZ angular power spectrum using the universal gas-density and temperature profile and the dark-matter halo mass function. The predicted power spectrum has no free parameters and fits all of the published hydrodynamic simulation results to better than a factor of two for  $2000 < l < 10000$ . We find that the angular power spectrum  $C_l$  scales as  $C_l \propto \sigma_8^7 (\Omega_b h)^2$  and is almost independent of all of the other cosmological parameters. This differs from the local cluster abundance studies, which give a relation between  $\sigma_8$  and  $\Omega_m$ . We also compute the covariance matrix of  $C_l$  using the halo model and find a good agreement relative to the simulations. We argue that the best constraint from the SZ power spectrum comes from  $l \sim 3000$ , where the sampling variance is sufficiently small and the spectrum is dominated by massive clusters above  $10^{14} h^{-1} M_\odot$  for which cooling, heating and details of star formation are not very important. We estimate how well we can determine  $\sigma_8 (\Omega_b h)^{2/7}$  with sampling-variance-limited observations and find that for a several-square-degree survey with arcminute resolution one should be able to determine  $\sigma_8$  to within a few percent, with the remaining uncertainty dominated by theoretical modeling. If the recent excess of the CMB power on small scales reported by CBI and BIMA experiments is due to the SZ effect, then we find  $\sigma_8 (\Omega_b h / 0.035)^{0.29} = 1.04 \pm 0.12$  at 95% confidence level (statistical) and with a residual 10% systematic (theoretical) uncertainty.

**Key words:** cosmology: theory — cosmic microwave background — dark matter — galaxies: haloes — galaxies: clusters: general — cosmological parameters

## 1 INTRODUCTION

Abundance of dark-matter halos and its redshift evolution have been recognized as an important cosmological test. For example, the local abundance of X-ray clusters can be used to constrain a combination of the matter-fluctuation amplitude and the matter density of the universe (e.g., White, Efstathiou, & Frenk 1993; Viana & Liddle 1996; Eke, Cole, & Frenk 1996; Kitayama & Suto 1997). Higher-redshift clusters can be used to break this degeneracy (e.g., Bahcall & Fan 1998), as well as constrain other cosmological parameters (Haiman, Mohr, & Holder 2001).

There are two major uncertainties in such analysis. One is the sample itself, which has to be carefully constructed to avoid any possible selection biases that can affect the final constraint. The other is the relation between observable quantities (e.g., X-ray temperature or flux) and the halo mass, which is related to the theoretical models. The latter uncertainty is particularly important as a small error in this relation can result in a significant effect on the final results. For example, the X-ray flux scales as gas-density squared and is dominated by the central regions, where complicated physical processes are taking place. This means that the relation between flux or flux-weighted temperature and the halo mass is not easily obtained from *ab-initio* numerical simulations, and one must resort to more empirical calibrations instead.

The Sunyaev–Zel’dovich (SZ) effect has some advantages

\* E-mail: komatsu@astro.princeton.edu

† E-mail: usej@princeton.edu

over X-ray in this respect. The SZ effect is caused by the cosmic microwave background (CMB) photons scattering off hot electrons in the intracluster medium, and the SZ flux is proportional to the projected electron-gas pressure, which is proportional to a product of electron number density and temperature along the line of sight. Relative to X-ray emission this has a larger contribution from the outer parts of the cluster, where the missing physics such as gas preheating or cooling in numerical simulations is less significant.

However, the SZ effect is very difficult to measure and currently only detections of already-known clusters exist (Birkinshaw 1999). It is likely that the first SZ detection in a random direction will not be that of a specific cluster, but of a field correlation function, or the angular power spectrum  $C_l$ , with several low signal-to-noise clusters contributing to the signal. Even if individual clusters are too faint to be detected with high statistical significance, the combined effect in  $C_l$  can be statistically significant. There have been several observational efforts in measuring the small-scale fluctuations, and upper-limits have been obtained by ATCA (Subrahmanyam et al. 1998), BIMA (Holzapfel et al. 2000; Dawson et al. 2001), SUZIE (Church et al. 1997; Ganga et al. 1997), and VLA (Partridge et al. 1997). Recently, CBI and BIMA experiments have reported statistically significant detections of the small-scale fluctuations at the level of  $15 - 20 \mu\text{K}$  on arcminutes angular scales (Mason et al. 2002; Dawson et al. 2002), and their results may already be providing the first detection of the SZ fluctuations (Bond et al. 2002).

There are other advantages of using power spectrum in addition to the higher statistical significance in a noisy map. One is that selection effects are less important than in a cluster survey, for which flux, surface brightness, and other selection criteria have to be carefully examined to avoid any biases. The other is that we do not have to measure the mass of individual haloes. As discussed above this is a dominant source of uncertainty in the local-mass-function determination from X-ray clusters and lack of a good calibration can lead to a 30% error on  $\sigma_8$ . Even if mass were determined from SZ flux, for which the central regions are less important, one would still need to include effects such as substructure, projections, ellipticity etc. As we argue in this paper using the SZ power spectrum instead of the number-count analysis is less sensitive to selection biases and can still give statistically significant results. It is true that the power spectrum does not use all of the information available, specially if one obtains the information on cluster redshifts. However, the SZ power spectrum provides quite powerful constraints on cosmological parameters already by itself and the small increase in statistical errors is more than compensated by the decrease in the systematic uncertainties. Thus initial experimental efforts should focus on the power spectrum as a more reliable method to determine the cosmological parameters.

There are of course other effects that contribute to fluctuations in this range of wavelengths. The SZ effect is the dominant contribution for  $l > 2000 - 4000$ , depending on its amplitude. The primary CMB dominates on the larger scales. Although the primary CMB confuses the SZ effect, we can reduce or eliminate it by observing at 217 GHz at which the SZ effect vanishes. Many of the current generation CMB experiments (such as CBI) operate at low frequencies, where the frequency dependence of CMB and the SZ effect is similar, and the two cannot be distinguished very well on this basis. Galactic emission (synchrotron, dust, or free-free) does not have much power on the small angular scales, and has a different frequency dependence from CMB. They are not likely to be a major source of contamination. We ignore the kinetic SZ effect,

as it is at least an order of magnitude smaller in power than the thermal SZ effect.

Point sources have a lot of small-scale power and are potentially more problematic contaminant. While we can easily identify bright (more than several- $\sigma$ ) point sources, we cannot identify the fainter ones, which will contaminate the SZ effect. This is particularly problematic for narrow frequency coverage experiments such as CBI, as we cannot use different frequency dependence of the point sources to separate the two components. We can still try to use opposite signatures between SZ and point sources as a way to distinguish them; the SZ effect is negative in flux at low frequencies, while point sources are positive. This results in a skewed one-point-distribution function. We can also use the difference in the shape of the correlation function, since more extended correlation in the SZ effect differs from the point sources. The SZ power spectrum scales roughly as  $l^{-2}$  while that of the point sources is constant, so the two can be distinguished. In practice noise and beam smoothing may make this analysis more complicated.

Within a few years, several experiments will likely measure the SZ effect with an arcminute angular resolution and the effective area of several square degrees. This has motivated us to revisit the predictions for the SZ angular power spectrum. Many analytic calculations exist in the literature (Cole & Kaiser 1988; Makino & Suto 1993; Atrio-Barandela & Mücke 1999; Komatsu & Kitayama 1999; Cooray 2000; Molnar & Birkinshaw 2000; Holder & Carlstrom 2001; Zhang & Pen 2001), as well as many hydrodynamic-simulation results (Scaramella, Cen, & Ostriker 1993; Persi et al. 1995; Refregier et al. 2000; Seljak, Burwell, & Pen 2001; da Silva et al. 2000; da Silva et al. 2001a; da Silva et al. 2001b; Springel, White, & Hernquist 2001; Refregier & Teyssier 2000; Zhang, Pen, & Wang 2002). The comparison between different simulations is difficult, as the parameters used differ, and the resulting power spectrum is extremely sensitive to the chosen parameters. Since massive clusters are at the tail of the dark-matter mass function, the r.m.s. mass fluctuations within a  $8 h^{-1} \text{Mpc}$  sphere,  $\sigma_8$ , is the most important parameter among the cosmological parameters. Komatsu & Kitayama (1999) have shown that the matter density of the universe is less important than  $\sigma_8$ .

Refregier et al. (2000) and Refregier & Teyssier (2000) have attempted to compare analytic predictions based upon the so-called ‘‘halo approach’’ (section 2) with their simulated power spectrum, finding a good agreement. This agreement is, however, partially built into their model; in their approach, the parameters such as upper and lower mass cut-off are chosen to agree with the simulations. Another free parameter used in the analytic modeling that cannot be obtained from these models is the mass-temperature normalization. Although a virial relation has often been used in this context, the overall amplitude is treated as a free parameter, and cannot be justified without a more detailed model. In this paper we develop a more refined analytic model and show that it reproduces the simulation results without any free parameters, at least at the level of the simulations disagreeing among themselves.

The main ingredients into the halo model are the dark-matter-halo mass function, the gas-density and the gas-temperature profiles. For the latter, we use an analytic gas and temperature profile model developed in our previous paper (Komatsu & Seljak 2001). We have shown that it reproduces well the simulation results in the outer parts of the cluster which are relevant for the SZ effect. This model fixes the normalization between mass and temperature by requiring that the gas and the dark-matter profiles agree with each other outside the gas core. Hydrodynamic simulations (e.g., Frenk et al. 1999) have shown that this assumption holds accurately. As a

result of this assumption and hydrostatic equilibrium the gas temperature declines in the outer parts of the cluster, which is also seen in the simulations (although it remains controversial in X-ray observations due to the faint levels of X-ray emission in the outer parts of the cluster). This model therefore reproduces the main features of the hydrodynamic simulations and can be viewed as the gas analog of the often-used NFW profile (Navarro, Frenk, & White 1997) for dark matter, at least outside the gas core where additional physics may play a role.

The structure of this paper is as follows. In § 2 we outline the “halo approach” to calculating the SZ angular power spectrum. In § 3 we derive the universal gas-density, gas-temperature, and gas-pressure profiles following the prescription described by Komatsu & Seljak (2001). In § 4 we predict the spectrum and compare it to the hydrodynamic simulations. We then investigate the dependence of the spectrum on various cosmological parameters. We also study the mass and redshift distribution of the spectrum. In § 5 we compute the covariance matrix of  $C_l$  by taking into account non-Gaussianity of the SZ fluctuations and compare these to the hydrodynamic simulations. In § 6 we show how well we can determine  $\sigma_8$  with realistic SZ observations using a likelihood analysis. We put constraints on a  $\Omega_m - \sigma_8$  plane using the recent CBI and BIMA data of the small-scale CMB fluctuations at  $l \sim 2000 - 6000$  (Mason et al. 2002; Dawson et al. 2002). In § 7 we quantify the theoretical uncertainty in our predictions. Finally, we summarize our results in § 8. The fiducial cosmological model in this paper is  $\Omega_m = 0.37$ ,  $\Omega_\Lambda = 0.63$ ,  $\Omega_b = 0.05$ ,  $h = 0.7$ ,  $w = -1.0$ ,  $n = 1.0$ , and  $\sigma_8 = 1.0$ .

## 2 HALO APPROACH TO THE SZ ANGULAR POWER SPECTRUM

To compute the angular power spectrum of the SZ effect we use the halo formalism (Cole & Kaiser 1988; Makino & Suto 1993; Atrio-Barandela & Mücke 1999; Komatsu & Kitayama 1999; Cooray 2000; Molnar & Birkinshaw 2000; Holder & Carlstrom 2001). For the angular scales of interest here,  $l > 300$ , the one-halo Poisson term dominates  $C_l$  even after the subtraction of local massive haloes (Komatsu & Kitayama 1999). We thus neglect the halo-halo correlation term throughout the paper.

The expression for  $C_l$  is given by

$$C_l = g_\nu^2 \int_0^{z_{\max}} dz \frac{dV}{dz} \int_{M_{\min}}^{M_{\max}} dM \frac{dn(M, z)}{dM} |\tilde{y}_l(M, z)|^2, \quad (1)$$

where  $g_\nu$  is the spectral function of the SZ effect ( $-2$  in the Rayleigh–Jeans limit) (Sunyaev & Zeldovich 1980),  $V(z)$  the comoving volume of the universe at  $z$  per steradian,  $dn(M, z)/dM$  the comoving dark-matter-halo mass function, and  $\tilde{y}_l(M, z)$  the 2D Fourier transform of the projected Compton  $y$ -parameter. The virial mass  $M$  used here and its mass function are described in more detail in section 2.1.

For the upper integration boundary of redshift it suffices to take  $z_{\max} = 10$  (figure 5). For the mass integration boundaries,  $M_{\min}$  and  $M_{\max}$ , we find that  $M_{\min} = 5 \times 10^{11} h^{-1} M_\odot$  and  $M_{\max} = 5 \times 10^{15} h^{-1} M_\odot$  suffice to get the integral to converge on all angular scales, whereas  $M_{\min} = 5 \times 10^{12} h^{-1} M_\odot$  is sufficient for  $l < 10^4$  (figure 6). Since the integrals converge the results are not subject to the specific choice of integration boundaries.

The 2D Fourier transform of the projected Compton  $y$ -parameter,  $\tilde{y}_l = \tilde{y}_l(M, z)$ , is given by

$$\tilde{y}_l = \frac{4\pi r_s}{l_s^2} \int_0^\infty dx x^2 y_{3D}(x) \frac{\sin(lx/l_s)}{lx/l_s}, \quad (2)$$

where  $y_{3D}(x)$  is the 3D radial profile of the Compton  $y$ -parameter (equation 7 in section 3). Note that  $y_{3D}(x)$  has a dimension of  $(\text{length})^{-1}$ , while  $\tilde{y}_l$  is dimensionless. In equation (2) we have used  $x$  as a scaled, non-dimensional radius,

$$x \equiv r/r_s, \quad (3)$$

where  $r_s = r_s(M, z)$  is a scale radius which characterizes the 3D radial profile and the corresponding angular wave number is

$$l_s \equiv d_A/r_s. \quad (4)$$

Here  $d_A = d_A(z)$  is the proper angular-diameter distance. The projection of the 3D profile onto the sky in equation (2) was done within the Limber’s approximation. In section 3, we derive  $y_{3D}(x)$  using the universal gas and temperature profile.

### 2.1 Dark-matter halo mass function

For the dark-matter halo mass function  $dn(M, z)/dM$  in equation (1) we use the universal mass function (Jenkins et al. 2001), which was derived from  $N$ -body simulations. We should be careful about the definition of “mass” when using the mass function derived from  $N$ -body simulations (e.g., White 2001; Seljak 2001; Hu & Kravtsov 2002). The mass of haloes in the simulations is usually not the virial mass  $M$  as defined in our analytic formulation (equation 1). Instead, the simulations usually use either the friend-of-friend (FOF) mass or the spherical overdensity (SO) mass to define the haloes. We use here the SO mass, as the FOF mass is difficult to interpret in the context of analytic formulation.

We define the SO mass,  $M_\delta$ , as the mass within the spherical region whose density is  $\delta$  times the critical density of the universe at  $z$   $\rho_c(z)$  (note that sometimes one uses instead the mass within the spherical region whose density is  $\tilde{\delta}$  times the mean mass density of the universe at  $z$ ,  $\rho_m(z) = \Omega_m(z)\rho_c(z)$ ; the two are related through  $\delta = \Omega_m(z)\tilde{\delta}$ ). Since  $N$ -body simulations give  $dn(M_\delta, z)/dM_\delta$ , we need to convert it into  $dn(M, z)/dM$ . We do this by calculating

$$\frac{dn(M, z)}{dM} = \frac{dM_\delta}{dM} \frac{dn(M_\delta, z)}{dM_\delta}. \quad (5)$$

For a given virial mass,  $M$ , we calculate  $M_\delta$  with equation (14) of Komatsu & Seljak (2001), and also evaluate  $dM_\delta/dM$  numerically.

We use equation (B3) of Jenkins et al. (2001), which explicitly uses  $\delta = 180\Omega_m(z)$  (mass density of haloes is 180 times the mean mass density of the universe at  $z$ ),

$$\begin{aligned} \frac{dn(M_\delta, z)}{dM_\delta} &= \Omega_m(0) \frac{\rho_c(0)}{M_\delta} \frac{d \ln \sigma^{-1}}{dM_\delta} \\ &\times 0.301 \exp\left(-|\ln \sigma^{-1} + 0.64|^{3.82}\right), \end{aligned} \quad (6)$$

where  $\sigma = \sigma(M_\delta, z)$  is the linear, r.m.s. mass fluctuations at a given redshift  $z$  within the top-hat filter. To compute  $\sigma$  we use the BBKS transfer function (Bardeen et al. 1986) with the baryonic correction made by Sugiyama (1995). The present-day critical density of the universe is  $\rho_c(0) = 2.775 \times 10^{11} h^2 M_\odot \text{Mpc}^{-3}$ . Note that we have defined the mass function as the comoving number density.

While the functional formula for the mass function in equation (6) was tested for just one cosmological model ( $\tau$ CDM model)

by Jenkins et al. (2001), it is essentially a non-smoothed version of their universal mass function valid for a broad range of models. Hu & Kravtsov (2002) have shown that the formula agrees with their simulated mass function as well which uses a different cosmological model. In addition, Evrard et al. (2002) have shown that their mass function for the SO mass haloes with  $\delta = 200$  agrees with the Jenkins et al.'s formula, once taking into account the mass definition properly (see also related discussion in Seljak 2001 and Hu & Kravtsov 2002). There is thus increasing evidence for the accuracy of Jenkins et al.'s mass function.

### 3 GAS-PRESSURE PROFILE OF HALOES

#### 3.1 Introduction

The 3D Compton  $y$ -parameter profile,  $y_{3D}(x)$ , is given by a thermal gas-pressure profile,  $P_{\text{gas}}(x)$ , through

$$\begin{aligned} y_{3D}(x) &\equiv \frac{\sigma_T}{m_e c^2} P_e(x) = \frac{\sigma_T}{m_e c^2} \left( \frac{2 + 2X}{3 + 5X} \right) P_{\text{gas}}(x) \\ &= 1.04 \times 10^{-4} \text{ Mpc}^{-1} \left[ \frac{P_{\text{gas}}(x)}{50 \text{ eV cm}^{-3}} \right], \end{aligned} \quad (7)$$

where  $P_e(x)$  is an electron-pressure profile,  $X = 0.76$  the primordial hydrogen abundance,  $\sigma_T$  the Thomson cross section,  $m_e$  the electron mass, and  $c$  the speed of light.

We may write  $P_{\text{gas}}(x)$  with a gas-density profile,  $\rho_{\text{gas}}(x)$ , and a gas-temperature profile,  $T_{\text{gas}}(x)$ , as

$$\begin{aligned} P_{\text{gas}}(x) &= \frac{3 + 5X}{4} \frac{\rho_{\text{gas}}(x)}{m_p} k_B T_{\text{gas}}(x) \\ &= 55.0 \text{ eV cm}^{-3} \\ &\times \left[ \frac{\rho_{\text{gas}}(x)}{10^{14} M_\odot \text{ Mpc}^{-3}} \right] \left[ \frac{k_B T_{\text{gas}}(x)}{8 \text{ keV}} \right], \end{aligned} \quad (8)$$

where  $m_p$  is the proton mass, and  $k_B$  the Boltzmann constant.

The aim of this section is to derive  $P_{\text{gas}}(x)$  following Komatsu & Seljak (2001). Pressure profile was one of the uncertainties in the previous work on the SZ power spectrum: most of the previous work uses a spherical-isothermal  $\beta$  model as a gas-density profile, with  $\beta$  fixed at  $2/3$  for simplicity (Makino & Suto 1993; Atrio-Barandela & Mucket 1999; Komatsu & Kitayama 1999; Molnar & Birkinshaw 2000; Holder & Carlstrom 2001); Cooray (2000) used an isothermal gas-density profile as predicted by Makino, Sasaki, & Suto (1998), which uses hydrostatic equilibrium between gas pressure and dark-matter potential, and is close to the  $\beta$  profile. The  $\beta$  profile does not, however, reproduce the simulation results in the outer parts of the haloes. The outer slope of the  $\beta$  model with  $\beta = 2/3$  scales as  $r^{-2}$ , being significantly shallower than the gas profile in simulations which, as we have argued, is similar to the dark-matter profile and asymptotically scales as  $r^{-3}$ . Since the SZ effect is sensitive to the outer parts of haloes, this can cause a significant error in the predictions.

There is a related uncertainty caused by the shallow ( $r^{-2}$ ) profile: one has to cut out the extension of gas in haloes at an arbitrary radius, otherwise one predicts too much power on large angular scales. We find that the previous predictions are unstable against this cut-off radius. This radius, which is a free parameter, has been assumed to be the virial radius; however, for isothermal gas assumed in the previous work this is *ad hoc*, as neither temperature nor density profile shows the abrupt cut-off at the virial radius in hydrodynamic simulations (Bryan & Norman 1998; Eke, Navarro, & Frenk 1998; Frenk et al. 1999). Instead, both the temperature

and the density decrease smoothly across the virial radius, and it is only at  $2 - 3$  times the virial radius that there seems to be an abrupt decrease of the temperature to the IGM value, the so-called shock radius (Bryan & Norman 1998).

Once the decline in profiles relative to the  $\beta$  model is included, the contribution from the outer parts of haloes to the SZ power spectrum converges well within the shock radius, and is thus independent of the outer cut-off of the profile. This is because requiring that the gas-density profile traces the dark-matter-density profile leads to  $\rho_{\text{gas}} \propto r^{-3}$  in the outer parts of the haloes. This by itself would give a logarithmically divergent gas-mass profile; however, since the temperature is also declining with radius, the resulting pressure profile is convergent. Hydrostatic equilibrium and the gas density tracing the dark-matter density make the gas temperature decrease with radius.

#### 3.2 Universal dark-matter-density profile

The universal NFW dark-matter-density profile (Navarro, Frenk, & White 1997) is

$$\rho_{\text{dm}}(x) = \frac{\rho_s}{x(1+x)^2}, \quad (9)$$

where  $x \equiv r/r_s$ ,  $r_s$  a scale radius, and  $\rho_s$  a scale density. While the exact shape in the inner parts is still uncertain (Moore et al. 1998; Jing & Suto 2000; Klypin et al. 2001), it does not affect the SZ effect, given the scales of interest here.

To specify the NFW profile, we need to specify a scale radius,  $r_s$ , as a function of mass and redshift. It is customary to specify the concentration parameter  $c$  instead of  $r_s$ ,

$$c(M, z) \equiv \frac{r_{\text{vir}}(M, z)}{r_s(M, z)} \approx \frac{10}{1+z} \left[ \frac{M}{M_*(0)} \right]^{-0.2}, \quad (10)$$

where  $r_{\text{vir}}(M, z)$  is the virial radius of haloes, and the last expression follows from Seljak (2000) with redshift evolution found by Bullock et al. (2001). The ‘‘non-linear mass’’ at  $z = 0$ ,  $M_*(0)$ , is a solution to  $\sigma(M) = \delta_c$ , where  $\sigma(M)$  is the present-day r.m.s. mass fluctuations within the top-hat filter,  $M$  the virial mass, and  $\delta_c$  the threshold overdensity of spherical collapse at  $z = 0$  (Lacey & Cole 1993; Nakamura & Suto 1997). We calculate the virial radius using the spherical collapse model,

$$r_{\text{vir}}(M, z) \equiv \left[ \frac{M}{(4\pi/3)\Delta_c(z)\rho_c(z)} \right]^{1/3}, \quad (11)$$

where  $\Delta_c(z)$  is a spherical overdensity of the virialized halo within  $r_{\text{vir}}$  at  $z$ , in units of the critical density of the universe at  $z$  (Lacey & Cole 1993; Nakamura & Suto 1997).

The exact form of  $c(M, z)$ , equation (10), is somewhat uncertain. There are various fitting formulae in the literature (Navarro, Frenk, & White 1997; Eke, Navarro, & Steinmetz 2001; Bullock et al. 2001; Seljak 2000; Cooray, Hu, & Miralda-Escudé 2000). In section 4 we study the effect of different concentration parameters on our predictions, in addition to using our fiducial concentration parameter dependence in equation (10). We find that the difference in concentration parameters does not affect our predictions, largely because the SZ effect is not sensitive to the central parts of haloes, where the profile shape makes most difference.

#### 3.3 Universal gas-pressure profile

To derive a gas-pressure profile  $P_{\text{gas}}(x)$  we make three assumptions: (1) hydrostatic equilibrium between gas pressure and dark-

matter potential due to the universal dark-matter density profile, (2) gas density tracing the universal dark-matter density in the outer parts of haloes, and (3) a constant polytropic equation of state for gas,  $P_{\text{gas}} \propto \rho_{\text{gas}}^\gamma$ . The assumption (3) is obviously just an approximation and can be justified only to the extent that it suffices to explain the observations or simulations. There is evidence for this assumption to fail within inner 5% of the virial radius, where X-ray observations indicate that temperature increases with radius (Allen, Schmidt, & Fabian 2001). Outside the core region, nevertheless, the constant polytropic index seems to suffice, at least in comparison to the simulations.

From these three assumptions one can obtain universal gas-density, gas-temperature, and gas-pressure profiles as

$$\rho_{\text{gas}}(x) = \rho_{\text{gas}}(0)y_{\text{gas}}(x), \quad (12)$$

$$T_{\text{gas}}(x) = T_{\text{gas}}(0)y_{\text{gas}}^{\gamma-1}(x), \quad (13)$$

and

$$P_{\text{gas}}(x) = P_{\text{gas}}(0)y_{\text{gas}}^\gamma(x). \quad (14)$$

Solving the hydrostatic equilibrium equation with the *ansatz* above, we find that the non-dimensional gas-density profile,  $y_{\text{gas}}(x)$ , has an analytic solution, and is given by (Komatsu & Seljak 2001)

$$y_{\text{gas}}(x) \equiv \left\{ 1 - B \left[ 1 - \frac{\ln(1+x)}{x} \right] \right\}^{1/(\gamma-1)}, \quad (15)$$

where the coefficient  $B$  is

$$B \equiv 3\eta^{-1}(0) \frac{\gamma-1}{\gamma} \left[ \frac{\ln(1+c)}{c} - \frac{1}{1+c} \right]^{-1}. \quad (16)$$

In appendix, we give exact formulae for the polytropic index,  $\gamma$ , and the mass–temperature normalization factor at the centre,  $\eta(0)$ . Here we provide instead useful fitting formulae:

$$\gamma = 1.137 + 8.94 \times 10^{-2} \ln(c/5) - 3.68 \times 10^{-3}(c-5), \quad (17)$$

and

$$\eta(0) = 2.235 + 0.202(c-5) - 1.16 \times 10^{-3}(c-5)^2. \quad (18)$$

These fitting formulae are valid for  $1 < c < 25$ . Since  $\gamma > 1$  and the density decreases with radius, the temperature also decreases with radius.

From  $\eta(0)$ , we can determine the central temperature,  $T_{\text{gas}}(0)$ , as

$$\begin{aligned} T_{\text{gas}}(0) &= \eta(0) \frac{4}{3+5X} \frac{Gm_p M}{3r_{\text{vir}}} \\ &= 8.80 \text{ keV } \eta(0) \left[ \frac{M/(10^{15} h^{-1} M_\odot)}{r_{\text{vir}}/(1 h^{-1} \text{ Mpc})} \right]. \end{aligned} \quad (19)$$

The central gas density,  $\rho_{\text{gas}}(0)$ , is determined by equation (21) below. We then compute the central gas pressure,  $P_{\text{gas}}(0)$ , by substituting  $\rho_{\text{gas}}(0)$  and  $T_{\text{gas}}(0)$  into equation (8). This completely specifies the gas-density, the gas-temperature, and the gas-pressure profiles of haloes and their normalizations.

We determine the amount of gas in haloes by requiring that the gas density in the outer parts of haloes is  $\Omega_b/\Omega_m$  times the dark-matter density. Unlike the  $\beta$  profile this is self-consistent, as our gas-density profile agrees with the dark-matter profile outside the gas core. The virial radius thus has no special importance, and the matching can be performed over a broad range of radii without affecting the results. We should reduce the gas fraction by the amount that has been converted to stars, which is of order 10–20% for massive clusters of interest here (Fukugita, Hogan, & Peebles 1998).

We choose not to apply this correction, so our predictions for the power spectrum are somewhat overestimated and the corresponding amplitude constraints underestimated. This however translates into only a few percent correction to the amplitude of  $\sigma_8$ .

We normalize the gas density at the virial radius,

$$\begin{aligned} \rho_{\text{gas}}(c) &= \rho_{\text{gas}}(0)y_{\text{gas}}(c) = \frac{\Omega_b}{\Omega_m} \rho_{\text{dm}}(c) \\ &= \frac{\Omega_b}{\Omega_m} \frac{M}{4\pi r_{\text{vir}}^3} \frac{c^2}{(1+c)^2} \left[ \ln(1+c) - \frac{c}{1+c} \right]^{-1}. \end{aligned} \quad (20)$$

We use this equation to obtain the central gas density,

$$\begin{aligned} \rho_{\text{gas}}(0) &= 7.96 \times 10^{13} M_\odot \text{ Mpc}^{-3} \\ &\times \left( \frac{\Omega_b h^2}{\Omega_m} \right) \frac{M/(10^{15} h^{-1} M_\odot)}{[r_{\text{vir}}/(1 h^{-1} \text{ Mpc})]^3} \\ &\times c^3 \left[ \frac{y_{\text{gas}}^{-1}(c)}{c^2(1+c)^2} \right] \left[ \ln(1+c) - \frac{c}{1+c} \right]^{-1}. \end{aligned} \quad (21)$$

## 4 PREDICTIONS FOR THE SZ ANGULAR POWER SPECTRUM

In this section, we predict the SZ angular power spectrum,  $C_l$ , by integrating equation (1), and compare the predictions with hydrodynamic simulations. We then study the sensitivity of  $C_l$  to various cosmological parameters. We also study mass and redshift distribution of  $C_l$ , finding that the power spectrum primarily probes massive haloes in a moderate redshift universe.

### 4.1 Comparison with hydrodynamic simulations

We begin by comparing our predictions for  $C_l$  with six hydrodynamic simulations (four independent codes), listed in table 1. Figure 1 compares our analytic predictions with the simulated power spectra.

The predictions generally agree with the simulations within a factor of two. We find the best agreement for the nominally highest-resolution ( $512^3$ ) simulation run by Zhang, Pen, & Wang (2002) using mesh-based MMH code (bottom-left panel of figure 1). The same code, but for different cosmological parameters and at lower ( $256^3$ ) resolution, agrees well below  $l < 10000$ , but lacks power above that (Seljak, Burwell, & Pen 2001) (top-left panel). Note that the number of realizations for this simulation was small, which explains lack of power at low  $l$  compared to even lower ( $128^3$ ) resolution used by Refregier et al. (2000) for the same code and the same cosmological parameters.

For the  $256^3$  simulation we have created more 2-d maps, covering the effective area of 1000 square degrees. We find that with more realizations  $C_l$  at low  $l$  increases, becoming into better agreement with Refregier et al. (2000). This indicates that the sampling variance is very large on large scales, but is significantly reduced above  $l \sim 2000 - 3000$ . With more realizations, one typically increases power on large scales, which explains some of the differences among different simulations (they differ in the effective simulated area significantly; see table 1). Even so most of the simulations are too small to include sufficient number of very massive halos and for these multiple maps from a single simulation do not reduce the sampling variance. This can explain why the simulations are still below the analytic model at low  $l$ . At least for MMH code, we find that the numerical resolution seems to be important at high

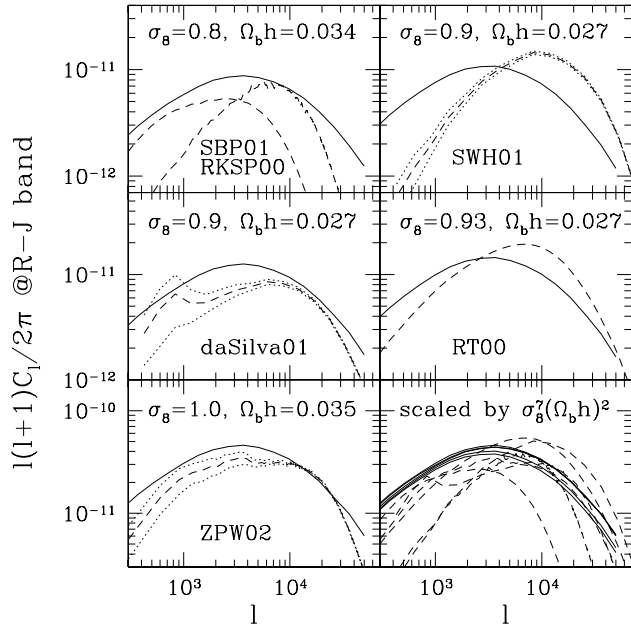


**Figure 1.** Comparison between the predicted SZ angular power spectra (solid) and the simulations (dashed; see table 1 for the meaning of the labels shown in each panel, and for the cosmological parameters used). The dotted lines indicate r.m.s. errors of the simulated power spectra. The bottom-right panel scales all the power spectra by  $\sigma_8^7 (\Omega_b h)^2$ . The agreement between the scaled power spectra indicates that this combination of cosmological parameters controls the amplitude of  $C_l$ .

$l$ , and it causes some of the discrepancy between our model and the MMH simulations.

The comparison with one of the two SPH simulations, da Silva et al. (2001b) using HYDRA code, shows a good agreement in shape, while the GADGET code (Springel, White, & Hernquist 2001) seems to predict more small-scale power above  $l \sim 5000$  compared to our predictions. We find that the shape of  $C_l$  of Springel, White, & Hernquist (2001) is similar to Refregier & Teyssier (2000), which uses a mesh-based hydrodynamic code, RAMSES, so the disagreement is unlikely to be due to simply SPH versus mesh-based codes. We note that the SPH simulation presented in Bond et al. (2002) also agrees in shape with Springel, White, & Hernquist (2001).

A possible explanation for the discrepancy is that some simulations such as MMH have not yet converged for very high  $l$ , while at low  $l$  sampling variance seems to be the most likely explanation. The discrepancy between our analytic model and GADGET and RAMSES could be caused by failure of our model at high  $l$ : clusters at higher redshift are less regular with more merging and substructure, which boosts  $C_l$  at high  $l$ . One way to account for this in analytic model would be to include subhalos within halos, but to properly calibrate this one would need to use hydrodynamic simulations. Here we argue that around  $l \sim 3000$  the theoretical model and the simulations seem to agree rather well, certainly within a factor of two or better. Any remaining discrepancy at low  $l$  could be due to insufficient sampling in simulations. Although a factor of two may sound like a large uncertainty in the  $C_l$  prediction, it translates into a rather small uncertainty in  $\sigma_8$ , as discussed below.

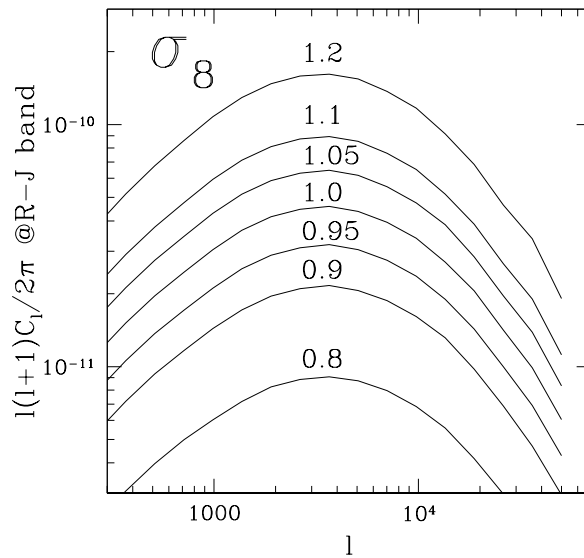


**Figure 2.** Dependence of the SZ angular power spectrum on  $\sigma_8$ . From top to bottom, the lines indicate  $\sigma_8 = 1.2, 1.1, 1.05, 1.0, 0.95, 0.9$ , and  $0.8$ , as shown in the figure.

## 4.2 Dependence on cosmological parameters

In previous work it has been argued that the SZ power spectrum is very sensitive to  $\sigma_8$  (Komatsu & Kitayama 1999; Seljak, Burwell, & Pen 2001; Zhang & Pen 2001; Zhang, Pen, & Wang 2002). Figure 2 shows this dependence within the analytic model. For example, a 40% change in  $\sigma_8$  causes one order of magnitude change in  $C_l$ , while a 10% change in  $\sigma_8$  causes a factor of two change. We find that  $C_l \propto \sigma_8^7$  provides a good description of this scaling (see also the bottom-right panel of figure 1). The strong dependence of  $C_l$  on  $\sigma_8$  indicates that even if the numerical simulations are uncertain at the level of a factor of two, this translates into less than 10% systematic uncertainty in  $\sigma_8$ .

This property of the SZ power spectrum should be compared with the current uncertainty in  $\sigma_8$  from the local cluster abundance studies, for which the systematic uncertainty is larger than 10% because of the uncertainty in the mass–temperature relation (e.g., Pierpaoli, Scott, & White 2001; Seljak 2001; Viana, Nichol, & Liddle 2002). Weak lensing (e.g., Van Waerbeke et al. 2002) and direct mass–temperature calibration may soon provide a more reliable method to determine  $\sigma_8 \Omega_m^{0.5}$  combination. On the other hand, we show below that  $C_l$  is not sensitive to  $\Omega_m$  in the range of current interest. This property can break the degeneracy between the two parameters.

Figure 3 shows dependence of  $C_l$  on  $\Omega_m$  assuming a flat universe, i.e.,  $\Omega_\Lambda = 1 - \Omega_m$ . While  $C_l \propto \Omega_m$  for  $\Omega_m > 0.4$ , we find that it is almost independent of  $\Omega_m$  for  $0.15 < \Omega_m < 0.4$ . This is because the comoving volume of the universe increases rapidly with  $\Omega_m$  decreasing in this region, canceling out the effect of  $\Omega_m$  on the dark-matter mass function. As this range of  $\Omega_m$  is favored by current observations,  $C_l$  is practically independent of  $\Omega_m$ .

Figure 4 shows dependence of  $C_l$  on equation of state  $w$ ,  $\Omega_b$ ,  $h$ , and  $n$ . While varying  $\Omega_b$  or  $h$ , we have fixed  $\Omega_b h$  at a fiducial value, 0.035, since we know that  $C_l$  scales as  $(\Omega_b h)^2$ . The figure

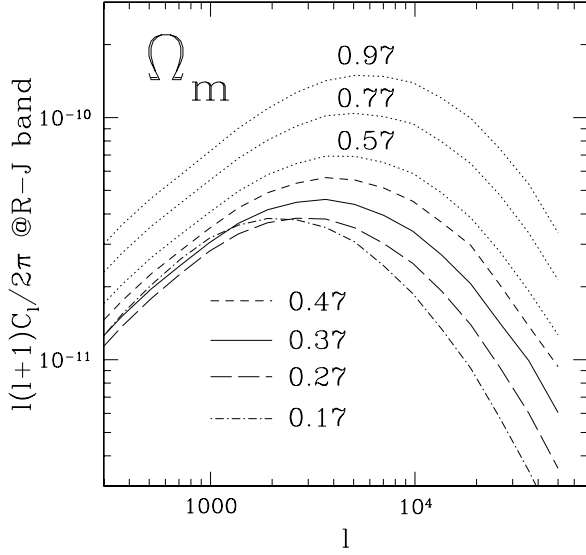


**Figure 3.** Dependence of the SZ angular power spectrum on  $\Omega_m$ . From top to bottom, the lines indicate  $\Omega_m = 0.97, 0.77, 0.57, 0.47, 0.37, 0.27,$  and  $0.17$ , as shown in the figure. While varying  $\Omega_m$ , we have assumed a flat universe, i.e.,  $\Omega_\Lambda = 1 - \Omega_m$ , and  $w = -1.0$ .

shows any residual dependence of  $C_l$  on  $\Omega_b$  or  $h$ . We find that  $C_l$  depends upon  $w$ ,  $\Omega_b$ ,  $h$ , or  $n$  very weakly compared to  $\sigma_8$  (compare figure 4 with figure 2). The only exception is if  $w > -2/3$ , which is however not favored by current observations (Bean & Melchiorri 2002).

We find that the dependence of overall amplitude of  $C_l$  on cosmological parameters for  $0.15 < \Omega_m < 0.4$  is well approximated by

$$\frac{l(l+1)C_l}{2\pi} \simeq 330 \mu\text{K}^2 \sigma_8^7 \left( \frac{\Omega_b h}{0.035} \right)^2 \quad (0.15 < \Omega_m < 0.4), \quad (22)$$

at the peak around  $l \sim 4000$ . As we have shown in figure 3,  $C_l$  is rather insensitive to  $\Omega_m$  over this region. A fit for  $\Omega_m > 0.4$  is given by

$$C_l \propto (\Omega_b h)^2 \Omega_m \sigma_8^{6.5 \Omega_m^{-0.2} - 0.9 \sigma_8} \quad (\Omega_m > 0.4). \quad (23)$$

### 4.3 Redshift and mass distribution

Figure 5 shows the redshift distribution of  $C_l$  for a given  $l$ ,

$$\frac{d \ln C_l}{d \ln z} \equiv \frac{z \frac{dV}{dz} \int dM \frac{dn(M,z)}{dM} |\tilde{y}_l(M,z)|^2}{\int dz \frac{dV}{dz} \int dM \frac{dn(M,z)}{dM} |\tilde{y}_l(M,z)|^2}. \quad (24)$$

We find that haloes at  $z \sim 1$  determine  $C_l$  at  $l \sim 3000$  (angular scales around  $3'$ ). Haloes at  $z \sim 2$  dominate  $C_l$  at  $l = 10000$ . Even haloes at  $z \sim 3$  have a non-negligible contribution to  $C_l$  for  $l > 10000$ .

Figure 6 shows the mass distribution of  $C_l$  for a given  $l$ ,

$$\frac{d \ln C_l}{d \ln M} \equiv \frac{M \int dz \frac{dV}{dz} \frac{dn(M,z)}{dM} |\tilde{y}_l(M,z)|^2}{\int dz \frac{dV}{dz} \int dM \frac{dn(M,z)}{dM} |\tilde{y}_l(M,z)|^2}. \quad (25)$$

We find that massive haloes between  $10^{14} h^{-1} M_\odot$  and  $10^{15} h^{-1} M_\odot$  dominate  $C_l$  at  $l = 3000$  with a peak at  $3 \times$

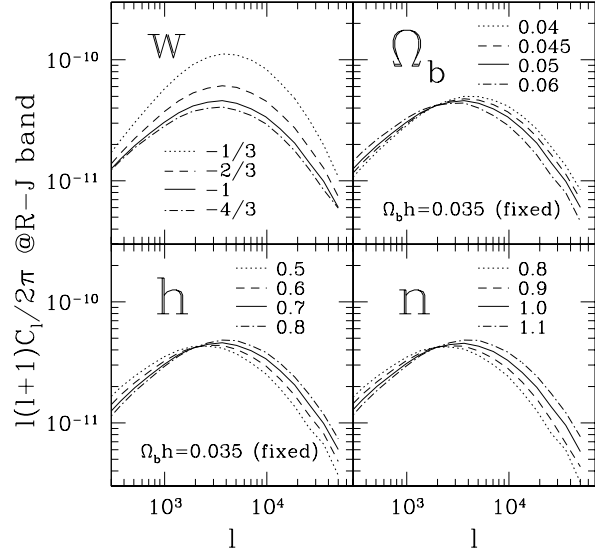


**Figure 4.** Dependence of the SZ angular power spectrum on the equation of state of the dark-energy component,  $w$ , the baryon density  $\Omega_b$ , the Hubble constant in units of  $100 \text{ km s}^{-1} \text{ Mpc}^{-1}$ ,  $h$ , and the primordial power-spectrum slope  $n$ . Values of each parameter are shown in each panel of the figure. While varying  $\Omega_b$  or  $h$ , we have  $\Omega_b h = 0.035$  fixed. The panels for  $\Omega_b$  and  $h$  are to show any residual dependence of  $C_l$  on these two parameters. This figure is to be compared with figure 2, showing how insensitive  $C_l$  is to  $w$ ,  $\Omega_b$ ,  $h$ , or  $n$  compared to  $\sigma_8$ .

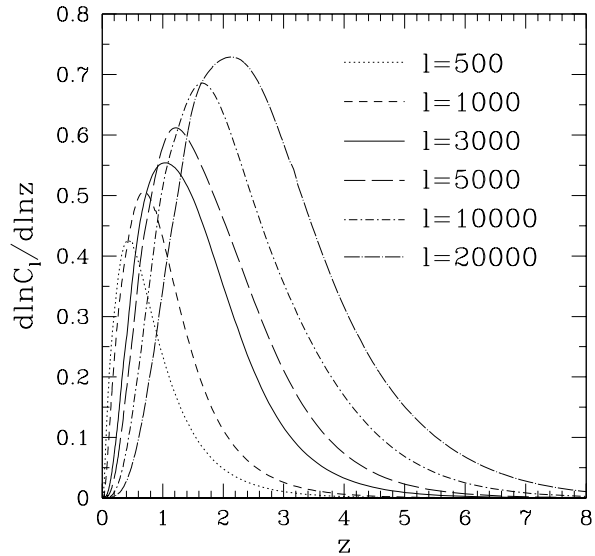


**Figure 5.** Redshift distribution of  $C_l$ . We plot  $d \ln C_l / d \ln z$ , equation (24), for a given  $l$ . From left to right it is shown  $l = 500, 1000, 3000, 5000, 10000,$  and  $20000$ , as indicated in the figure.

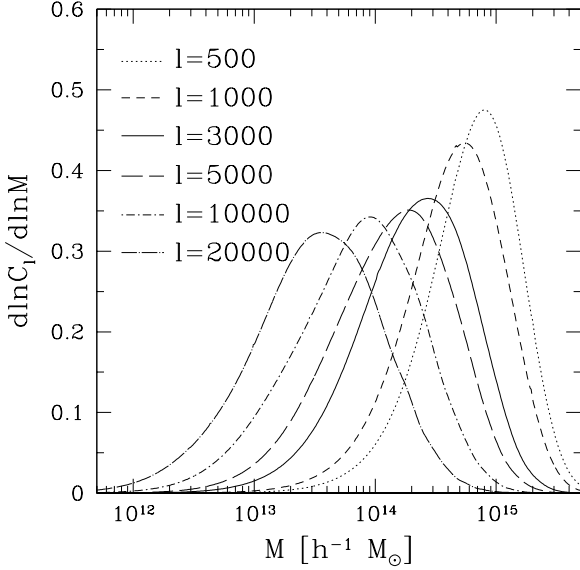


**Figure 6.** Mass distribution of  $C_l$ . We plot  $d \ln C_l / d \ln M$ , equation (25), for a given  $l$ . From right to left it is shown  $l = 500, 1000, 3000, 5000, 10000$ , and  $20000$ , as indicated in the figure.

$10^{14} h^{-1} M_\odot$ . For  $l = 1000$  the peak is at  $5 \times 10^{14} h^{-1} M_\odot$ , while for  $l = 10000$  at  $10^{14} h^{-1} M_\odot$ . The large-angular-scale  $C_l$  is thus sensitive to the presence of very massive and rare haloes, which explains why the sampling variance is so large on large scales. Much smaller angular scales ( $< l' < l > 10000$ ) receive significant contribution from smaller mass haloes, where uncertain physics of gas cooling, heating, or star formation makes predictions unreliable; however, for the angular scales of  $2' - 4'$  the dominant contribution is from massive ( $10^{14} - 10^{15} h^{-1} M_\odot$ ) clusters for which these uncertainties are small and which are still so abundant that the sampling variance is small. Fortunately, this is precisely the range targeted by the next generation CMB experiments.

## 5 COVARIANCE MATRIX OF THE SZ ANGULAR POWER SPECTRUM

To determine the cosmological parameters from the power spectrum we need to know its covariance matrix. If fluctuations are Gaussian, then we can calculate the variance from the spectrum itself. If fluctuations are non-Gaussian, then the covariance matrix is no longer diagonal. In this case we need to know not only  $C_l$ , but also specific configurations of the angular trispectrum, the harmonic transform of the four-point correlation function, to estimate the covariance matrix.

The SZ fluctuations observed in the hydrodynamic simulations are very non-Gaussian (Seljak, Burwell, & Pen 2001; Zhang, Pen, & Wang 2002; White, Henquist, & Springel 2001). The scatter among the  $C_l$  estimates is large, especially on large scales, and the estimates are strongly correlated. We must thus calculate the full covariance matrix, taking into account the non-Gaussianity. Here we will use both the halo approach (Cooray 2001), and the hydrodynamic simulations (Seljak, Burwell, & Pen 2001), to develop a reliable method for covariance matrix calculation.

The covariance matrix of  $C_l, M_{l'}$ , is given by (Cooray 2001)

$$\begin{aligned} M_{ll'} &\equiv \langle (C_l^{\text{obs}} - C_l) (C_{l'}^{\text{obs}} - C_{l'}) \rangle \\ &= f_{\text{sky}}^{-1} \left[ \frac{2(C_l)^2}{2l+1} \delta_{ll'} + \frac{T_{ll'}}{4\pi} \right], \end{aligned} \quad (26)$$

where the angular bracket denotes the ensemble average,  $f_{\text{sky}}$  is a fraction of the sky covered by an experiment ( $f_{\text{sky}} = 1$  for all sky),  $C_l^{\text{obs}}$  the observationally measured power spectrum, and  $C_l$  the theoretically predicted power spectrum (equation 1). Note that  $\langle C_l^{\text{obs}} \rangle = C_l$ . The second term in the r.h.s. represents the trispectrum contribution.

### 5.1 Halo approach to the angular trispectrum

In this section we calculate  $M_{ll'}$ , equation (26), using the halo approach, and compare it with the hydrodynamic simulations. An angular-trispectrum configuration is represented by a quadrilateral, and is characterized by four sides and one diagonal (Hu 2001). Among the trispectrum configurations, those which constitute two lines whose lengths are  $l$  and  $l'$ , respectively, and have zero diagonal, determine the power-spectrum covariance matrix. We denote these as  $T_{ll'}$  (equation 26).

Using the halo approach one obtains for the Poisson term which dominates the trispectrum (Cooray 2001),

$$\begin{aligned} T_{ll'} &= g_\nu^4 \int_0^{z_{\text{max}}} dz \frac{dV}{dz} \int_{M_{\text{min}}}^{M_{\text{max}}} dM \frac{dn(M, z)}{dM} \\ &\quad \times |\tilde{y}_l(M, z)|^2 |\tilde{y}_{l'}(M, z)|^2, \end{aligned} \quad (27)$$

where all the quantities have the same meaning as in equation (1). It follows from equation (26) that  $(4\pi f_{\text{sky}})^{-1} T_{ll'}$  determines the non-diagonal terms of  $M_{ll'}$ . Figure 7 shows  $T_{ll'}$  divided by  $C_l C_{l'}$ . To make it represent a ratio of the ‘‘non-Gaussian error’’ (the second term in  $M_{ll'}$  of equation 26) to the ‘‘Gaussian error’’ (the first term) we have plotted  $T_{ll'}/(C_l C_{l'})$  multiplied by  $\sqrt{(2l+1)(2l'+1)}/8\pi$ , which is this ratio when  $l = l'$ . We find that the ratio decreases with  $l$  as  $l^{-0.95}$ , or equivalently,  $T_{ll} \propto l^{-1.95} (C_l)^2$ , for  $l \gtrsim 10^3$ .

Figure 7 also shows how  $M_{ll'}$  scales with  $l$  for a given  $l'$ . In the limit of  $T_{ll} \ll (C_l)^2$ , the plotted quantity in figure 7 reduces to the correlation coefficient of  $C_l, r_{ll}$ , given by

$$\begin{aligned} r_{ll'} &\equiv \frac{M_{ll'}}{\sqrt{M_{ll} M_{l'l'}}} \\ &\approx \frac{\sqrt{(2l+1)(2l'+1)}}{8\pi} \frac{T_{ll'}}{C_l C_{l'}} \quad (T_{ll} \ll C_l^2). \end{aligned} \quad (28)$$

As  $T_{ll'}/(C_l C_{l'})$  varies slowly with  $l$  for a given  $l'$ ,  $C_l$  and  $C_{l'}$  remain highly correlated even for a large value of  $|l - l'|$  (Cooray 2001). Because of this reason binning does not reduce the error bars as much as it would for Gaussian fluctuations.

### 5.2 Comparison with the simulated error bars

To compare the predicted error bars of  $C_l$  with the simulated ones one must take into account binning or band averaging that the simulations use to produce  $C_l$ . If the binned  $C_l$  at a given  $l$  is the average of  $C_l$  between  $l - \Delta l / 2 \leq l \leq l + \Delta l / 2$ , then the covariance matrix is

$$M_{ll'} \approx f_{\text{sky}}^{-1} \left[ \frac{2(C_l)^2}{(2l+1)\Delta l} \delta_{ll'} + \frac{T_{ll'}}{4\pi} \right]. \quad (29)$$



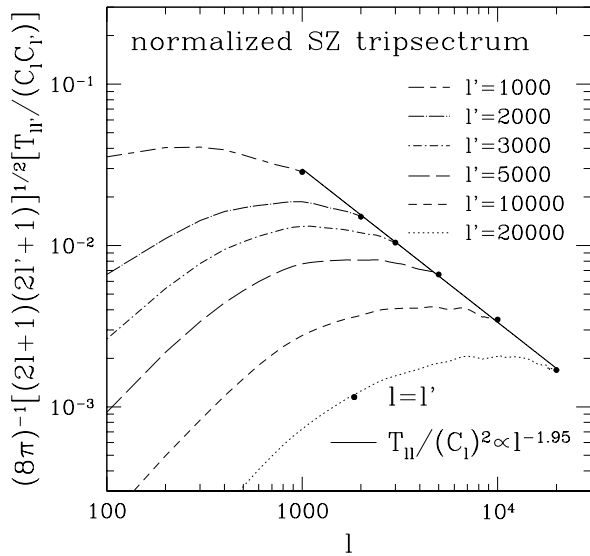


**Figure 7.** The SZ angular trispectrum,  $T_{ll'}$ , multiplied by  $\sqrt{(2l+1)(2l'+1)}/C_l C_{l'}$ . From top to bottom it is shown  $l' = 1000, 2000, 3000, 5000, 10000,$  and  $20000$ , as indicated in the figure. The solid line shows  $\propto l^{-0.95}$ , which means that the ratio of the non-Gaussian error to the Gaussian error decreases with  $l$  as  $l^{-0.95}$ , and  $T_{ll}$  scales as  $\propto l^{-1.95}(C_l)^2$ . The plotted quantity reduces to the correlation coefficient of  $C_l$  in the limit of  $T_{ll} \ll (C_l)^2$ .

Here, we have assumed that  $\Delta l \ll l$ . Since both  $C_l$  and  $T_{ll'}$  are sufficiently smooth, the binning does not affect the values of  $C_l$  and  $T_{ll'}$  as long as  $\Delta l \ll l$ . We find that  $\Delta l/l < 0.1$  suffices for this approximation to hold.

Figure 8 compares the predicted fractional errors of  $C_l$ ,  $\Delta C_l/C_l \equiv \sqrt{M_{ll}}/C_l$ , with the simulated ones. We find that the predictions agree with the simulations within a factor of two, similar to the agreement we have found for the spectrum itself. There is no clear trend in the residuals and we both overpredict and underpredict the variance compared to the simulations. Since the variance is very sensitive to the sampling errors, it is possible that some of the discrepancy is caused by insufficient sampling in the simulations. Figure 8 also plots Gaussian approximation to the errors, showing that our predictions give a significant improvement over the Gaussian approximation. We have also compared the predicted correlation coefficient,  $r_{ll'}$  (equation 28), with the simulations of Seljak et al. (2001), finding a good agreement between the two and confirming that for high  $l$  the neighboring bins in  $C_l$  are strongly correlated if the binning is sufficiently broad for the trispectrum term to dominate. Proper modeling of cross-correlations between the bins is essential for the parameter-error estimation and for the proper treatment of the statistical significance of results.

## 6 DETERMINATION OF POWER-SPECTRUM AMPLITUDE

In this section, we analyze how well we can determine  $\sigma_8$  by measuring the SZ angular power spectrum with realistic observations, and apply it to the recent CBI results (Mason et al. 2002).

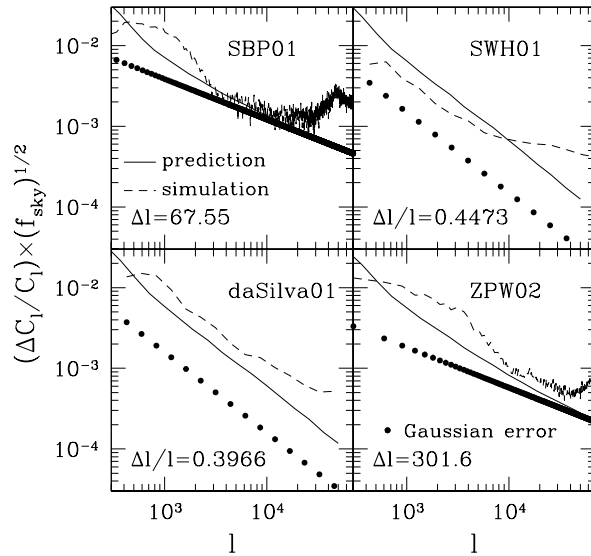


**Figure 8.** Predicted fractional r.m.s. errors of  $C_l$ ,  $\Delta C_l/C_l \equiv \sqrt{M_{ll}}/C_l$ , in comparison with the simulated errors (see table 1 for the meaning of the labels shown in each panel, and for the cosmological parameters used). We have multiplied the simulated errors by the square-root of a fraction of the sky covered by the simulations,  $f_{\text{sky}}$ . The solid lines show the predicted fractional errors, while the dashed lines show the simulated ones. The filled circles show Gaussian approximation to the fractional errors,  $\simeq (l\Delta l)^{-1/2}$  for  $l \gg 1$ , where  $\Delta l$  is the binning size shown in each panel. The predicted errors agree with the simulated ones within a factor of two, providing a significant improvement over the Gaussian approximation.

We perform a least-square fitting to  $C_l$  by calculating  $\chi^2$ ,

$$\chi^2 \equiv \sum_{l \leq l'} (\hat{C}_l - C_l) (M^{-1})_{ll'} (\hat{C}_{l'} - C_{l'}), \quad (30)$$

where  $\hat{C}_l$  is a reference power spectrum which uses the fiducial cosmological parameters, or the actual CBI data. We determine the confidence levels of the parameter estimation by calculating  $\Delta\chi^2$ .

We vary  $\Omega_m$  and  $\sigma_8$ , i.e.,  $\chi^2 = \chi^2(\Omega_m, \sigma_8)$ . We fix the other parameters at the fiducial values,  $\Omega_\Lambda = 1 - \Omega_m$ ,  $\Omega_b = 0.05$ ,  $h = 0.7$ ,  $w = -1.0$ , and  $n = 1.0$ . For a given set of cosmological parameters, we calculate  $C_l$  and  $M_{ll'}$  and then obtain  $\chi^2$ . By approximating probability distribution function of  $C_l$  with a Gaussian we have  $\Delta\chi^2 = 2.30, 6.17,$  and  $11.8$  for 68.3%, 95.4%, and 99.7% confidence levels (C.L.), respectively.

First, we assume that experiments are sampling-variance limited for  $2000 < l < 3000$ , or  $2000 < l < 5000$ ; thus, we consider a few arcminutes angular resolution and ignore instrumental noise. To save computational time we do not evaluate equation (30) at every  $l$ , but at 10 points for  $2000 < l < 3000$ , or 20 points for  $2000 < l < 5000$ . This choice gives  $\Delta l = 111$  and  $158$ , respectively, in equation (29). Both  $C_l$  and  $T_{ll'}$  are smooth so that this is a good approximation.

For the sky coverage we consider  $1 \text{ deg}^2$  or  $10 \text{ deg}^2$  survey of the sky. These parameters are characteristic for the on-going or forthcoming experiments: CBI (Padin et al. 2001) for  $2000 < l < 3000$  and  $1 \text{ deg}^2$ , SZA (Holder & Carlstrom 2001) for  $2000 < l < 3000$  and  $10 \text{ deg}^2$ , AMIBA (Zhang, Pen, & Wang 2002) or

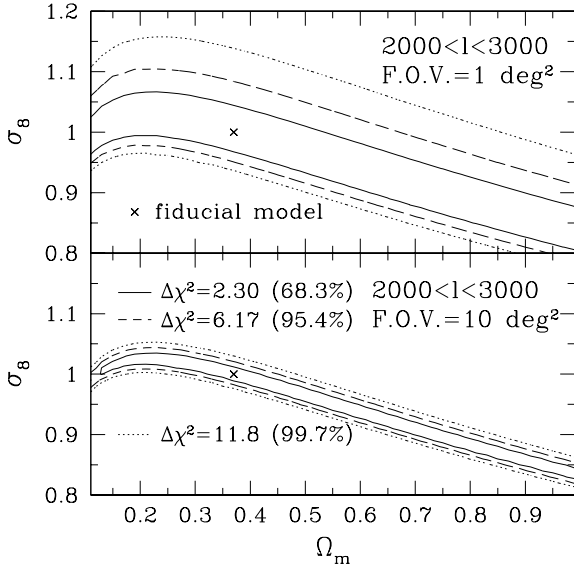


**Figure 9.** Contours showing how well we can determine  $\sigma_8$  against  $\Omega_m$  by measuring the SZ angular power spectrum with realistic observations. We consider those observations which measure  $C_l$  between  $2000 < l < 3000$ , and survey  $1 \text{ deg}^2$  (top panel), or  $10 \text{ deg}^2$  (bottom panel) of the sky. The top panel is similar to the CBI experiment and the bottom panel to the SZA experiment. The solid line shows  $\Delta\chi^2 = 2.30$  (68.3% C.L.), the dashed line  $\Delta\chi^2 = 6.17$  (95.4% C.L.), and the dotted line  $\Delta\chi^2 = 11.8$  (99.7% C.L.). The cross marks the fiducial cosmological model. We find that the contour is very sensitive to  $\sigma_8$ , yet almost independent of  $\Omega_m$  at around  $\Omega_m \sim 0.2$  (see also section 4). We find that a CBI-type observation should be able to determine  $\sigma_8$  to within 10% at  $2\sigma$ , while a SZA-type to within 5% at the same level.

ACT (Lyman Page, private communication) for  $2000 < l < 5000$  and  $10 \text{ deg}^2$ . AMIBA and ACT experiments are actually going to survey about  $100 \text{ deg}^2$  of the sky, so that the actual constraints to be obtained from these experiments would be better than we show here.

Figure 9 shows  $\chi^2$  on a  $\Omega_m - \sigma_8$  plane for the  $2000 < l < 3000$  region. The solid line shows  $\Delta\chi^2 = 2.30$  (68.3% C.L.), the dashed line  $\Delta\chi^2 = 6.17$  (95.4% C.L.), and the dotted line  $\Delta\chi^2 = 11.8$  (99.7% C.L.). The top panel uses  $1 \text{ deg}^2$  of the sky, close to the CBI experiment (if it is sampling-variance limited), while the bottom panel uses  $10 \text{ deg}^2$  of the sky, close to the SZA experiment. We find that the contours are very sensitive to  $\sigma_8$  and almost independent of  $\Omega_m$  for  $0.15 < \Omega_m < 0.4$  (Komatsu & Kitayama 1999). This is consistent with what we have previously shown in section 4 (see equation 22). While for one degree sky coverage the sampling-variance error is similar to the systematic (theoretical) error (10% at the 95% confidence level), a 10-times larger survey like SZA with the same angular resolution should be able to determine  $\sigma_8$  to within 5% at the same level, so that at that point the errors will be dominated by the theoretical uncertainty rather than by statistics.

Figure 10 shows constraints on a  $\Omega_m - \sigma_8$  plane which would be obtained with ACT or AMIBA, whose angular resolution is  $1' - 2'$ . The figure uses  $2000 < l < 5000$  with  $1 \text{ deg}^2$  (top panel) or  $10 \text{ deg}^2$  (bottom panel) sky coverage. We find that the statistical error on  $\sigma_8$  is extremely small for a  $10 \text{ deg}^2$  survey. Surveys such

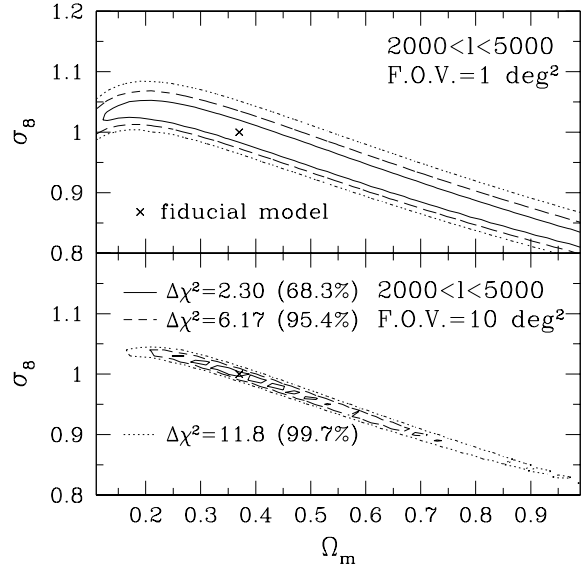


**Figure 10.** The same figure as figure 9, but for  $2000 < l < 5000$ . We find that statistical errors on  $\sigma_8$  are very small for a  $10 \text{ deg}^2$  survey, showing that ACT or AMIBA experiments which survey about  $100 \text{ deg}^2$  of the sky determine  $\sigma_8$  with theoretical-uncertainty-limited accuracy ( $\sim 10\%$ ). A  $1 \text{ deg}^2$  survey shown in the top panel is sufficient enough to determine  $\sigma_8$  with that accuracy.

as ACT or AMIBA covering about  $100 \text{ deg}^2$  of the sky will determine  $\sigma_8$  with accuracy limited by the theoretical uncertainty. This is currently at a  $\sim 10\%$  level and obviously more theoretical work should improve it in order for the power of the upcoming CMB experiments to be maximally exploited. It is of course still useful to cover such a large area of the sky, since this will allow us to use a bootstrap error determination without relying on the simulations.

Recently, CBI and BIMA announced detections of CMB power at  $l \sim 2000 - 6000$ , which at face value are inconsistent with the primary CMB alone (Mason et al. 2002; Dawson et al. 2002). Figure 11 compares the CBI and BIMA data (light-gray shaded area, which assumes Gaussian errors) to the predicted SZ angular power spectra for  $\sigma_8 = 0.95, 1.05, \text{ and } 1.15$  (thin solid lines). We also show the primary CMB anisotropy for the fiducial cosmological model (dashed line), and the sum of the two for  $\sigma_8 = 1.05$  (thick solid line). The predicted non-Gaussian errors are shown for  $\sigma_8 = 1.05$  (dark-gray shaded area). We have included the instrumental-noise power spectrum in the non-Gaussian errors by using the noise power spectrum of  $l(l+1)C_l/(2\pi) = 500, 1000, 1500, \text{ and } 3000 \mu\text{K}^2$  for the CBI bins, and  $720 \text{ and } 2000 \mu\text{K}^2$  for the BIMA bins. We have assumed the sky coverage of  $1 \text{ deg}^2$  for CBI and  $0.1 \text{ deg}^2$  for BIMA. From the figure one can see that the data favor  $\sigma_8 \sim 1$  models, and the predicted power spectra can explain the detected excess power reasonably well.

We fitted the data to the predicted SZ angular power spectrum using the four bins shown in figure 11 and computing  $\chi^2$  from equation (30). We compute the covariance matrix using equation (29) with the bin-size of  $\Delta l = 565, 378, 612, 1000, 2870, \text{ and } 4150$  for each bin. For example, we have obtained r.m.s. error of  $327, 398, 373, 425, 370, \text{ and } 299 \mu\text{K}^2$  at each bin for  $\sigma_8 = 1.05$ . The cross-correlation between the bins is most significant for the

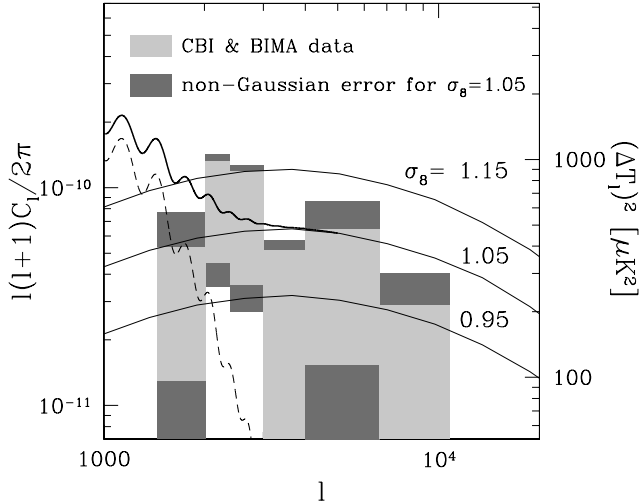


**Figure 11.** The CBI (Mason et al. 2002) and BIMA (Dawson et al. 2002) data with Gaussian errors (light-gray shaded area), the predicted SZ angular power spectra for  $\sigma_8 = 0.95, 1.05,$  and  $1.15$  (thin solid lines), the primary CMB anisotropy for the fiducial cosmological model (dashed line), and the sum of the two for  $\sigma_8 = 1.05$  (thick solid line). The dark-shaded area gives non-Gaussian errors predicted for  $\sigma_8 = 1.05$ .

first bin, for which the correlation coefficients with the other 3 CBI bins are 0.46, 0.41, and 0.29. The remaining 3 coefficients are below 0.3. Figure 12 shows confidence-level contours on the  $\Omega_m - \sigma_8$  plane for the CBI and BIMA data. The top panel (a) assumes that the detection of the excess power in the all bins is entirely due to the SZ effect (i.e., we ignore the primary CMB anisotropy). We find  $\sigma_8(\Omega_b h/0.035)^{2/7} = 1.04 \pm 0.12$  at 95% confidence limit for  $0.1 < \Omega_m < 0.5$ .

The cluster abundance and cosmic-shear constraints are also shown in the figure as  $\sigma_8 \Omega_m^{0.5} = 0.45 \pm 0.1$ , which roughly summarizes the current (systematic dominated) uncertainty from these methods. Combining the two can break the degeneracy between  $\sigma_8$  and  $\Omega_m$  and is leading to  $\sigma_8 \sim 1, \Omega_m \sim 0.2$ . One should be cautious not to overinterpret this conclusion, since systematic effects in both are still very large and could affect the parameter determination.

The bottom panel (b) assumes that the  $l \sim 1700$  bin is affected by the primary CMB anisotropy, while the other bins are entirely due to the SZ effect. We assume that the primary CMB is  $400 \mu\text{K}^2$  at the first bin, roughly consistent with the best-fitting theoretical curve, and is negligible in the other three bins. In principle we should change the primary CMB as well as we change the cosmological parameters; however, for simplicity we just use  $400 \mu\text{K}^2$  regardless of the cosmological parameters. We find a similar constraint on the  $\Omega_m - \sigma_8$  plane to the panel (a). In general, the CBI and BIMA data are consistent with detection of the SZ fluctuations, and imply  $\sigma_8(\Omega_b h/0.035)^{2/7} = 1.04 \pm 0.12$ , but a somewhat larger survey is needed to confirm this interpretation. The good news is that with a survey just a few times the survey area of CBI one should be able to determine  $\sigma_8$  with an accuracy com-

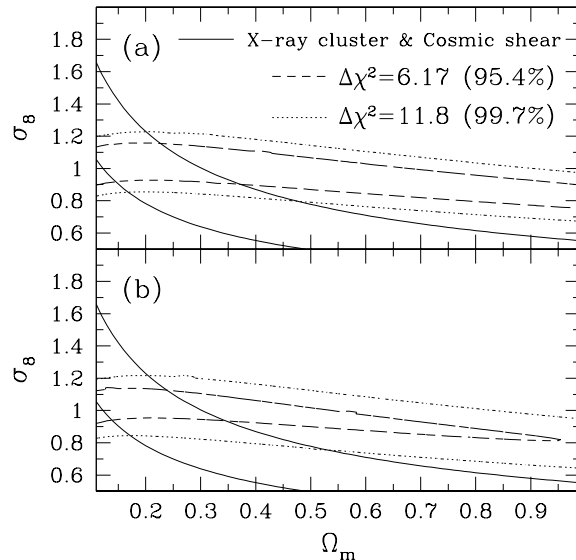


**Figure 12.** The CBI and BIMA constraints on the  $\Omega_m - \sigma_8$  plane. The top panel (a) assumes that all the data shown in figure 11 are entirely due to the SZ effect. The dashed line shows  $\Delta\chi^2 = 6.17$  (95.4% C.L.) while the dotted line  $\Delta\chi^2 = 11.8$  (99.7% C.L.). The cluster abundance and cosmic-shear constraints are shown in the figure as  $\sigma_8 \Omega_m^{0.5} = 0.45 \pm 0.1$ , which roughly summarizes the current uncertainty from these methods. The bottom panel (b) assumes that the first bin of the CBI data is affected by the primary CMB anisotropy. In both cases, we find  $\sigma_8(\Omega_b h/0.035)^{2/7} = 1.04 \pm 0.12$  at the 95.4% confidence level for  $0.1 < \Omega_m < 0.5$ .

parable to or better than any other current observations and with a different, and perhaps smaller, systematic uncertainty.

## 7 UNCERTAINTIES IN THE PREDICTIONS

The predictions are very sensitive to the halo mass function, so we investigate how the prediction changes if using different formulae in the literature. We compare four different predictions for  $C_l$  computed with four different formulae for the mass function: (JB3) Jenkins et al.’s  $\tau$ CDM mass function that uses the SO mass with  $\delta = 180\Omega_m(z)$  (Jenkins et al. 2001), (J9) Jenkins et al.’s universal mass function that uses the FOF mass (equation 9 of Jenkins et al. 2001) and includes smoothing which may systematically increase the mass function in the exponential tail (Hu & Kravtsov 2002), (HV) Evrard et al.’s Hubble-volume mass function which uses the SO mass with  $\delta = 200$  (Evrard et al. 2002), and (PS) Press & Schechter’s mass function which uses the virial mass (Press & Schechter 1974) (this one is of interest just for historical comparison). As Jenkins et al. (2001) note that the FOF mass they use corresponds to the SO mass with  $\delta = 180\Omega_m(z)$ , we use the SO mass to calculate the mass function of (J9).

The top-left panel (a) of figure 13 compares  $C_l$  computed with the four different mass functions. We find a very good agreement between (JB3) and (HV), while (J9) predicts higher amplitude. Hu & Kravtsov (2002) have also found that the mass function of (J9) predicts too many high-mass haloes to agree with their  $N$ -body simulations, and concluded that the smoothing used for deriving (J9) causes the high-mass halo abundance to increase anomalously.

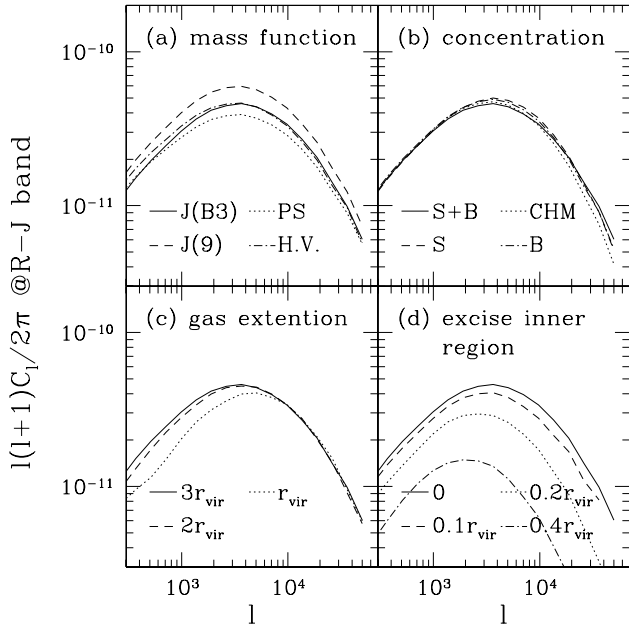


**Figure 13.** Theoretical uncertainty in the SZ angular power spectrum. **(a)** Uncertainty in the dark-matter-halo mass function. The solid line shows the prediction with Jenkins et al.’s  $\tau$ CDM mass function (equation 6), the dashed line Jenkins et al.’s universal mass function (equation 9 of Jenkins et al. (2001)), and the dot-dashed line Evrard et al.’s Hubble-volume mass function (Evrard et al. 2002). For comparison, the dotted line plots the prediction with Press & Schechter’s mass function (Press & Schechter 1974). **(b)** Uncertainty in the concentration parameter. **(c)** Uncertainty in the hot-gas extension in haloes. The solid line shows  $C_l$  with the hot-gas extension cut out at 3 times the virial radius, the dashed line at 2 times the virial radius, and the dotted line at the virial radius. **(d)** Uncertainty in the inner gas-pressure profile. The solid line shows  $C_l$  with no excision, the dashed line shows the one with the region interior to 10% of the virial radius excised, the dotted line 20% of the virial radius, and the dot-dashed line 40% of the virial radius. The dominant contribution to the spectrum is from 20 – 40% of the virial radius

Jenkins et al. (2001) have explained this in their paper: when deriving (J9), they are mainly interested in small-mass haloes for which the smoothing is less significant. Press & Schechter’s mass function predicts lower amplitude and underestimates the abundance of high-mass haloes compared with  $N$ -body simulations (Jenkins et al. 2001). As the SZ effect is dominated by the high-mass haloes, we should not use (J9) and (PS), but (JB3) or (HV).

Since there is no single expression for the concentration parameter  $c$  (see equation 10 for definition) we need to quantify how much uncertainty in  $C_l$  is due to the uncertainty in the concentration parameter. To quantify this, we use four different formulae for the concentration parameter: (S+B) power-spectrum-determined concentration parameter at  $z = 0$  (Seljak 2000) but evolved by  $(1+z)^{-1}$ , for which evolution has been measured in  $N$ -body simulations (Bullock et al. 2001), (S) power-spectrum determination with the non-linear mass evaluated at  $z$ , (B) halo determination of the concentration parameter (Bullock et al. 2001) and (CHM) a different power-spectrum-determined concentration parameter (Cooray, Hu, & Miralda-Escudé 2000). The top-right panel (b) of figure 13 shows the predictions computed with the four different concentration parameters. We find that the uncertainty in the concentration parameter has little effect on  $C_l$ .

How sensitive are the results to the outer radius of the gas profile (shock radius), where the gas temperature rapidly drops to IGM values? Previous work on a gas profile has assumed that the hot gas in haloes extends only up to the virial radius, but numerical simulations suggest a smooth decrease in temperature at least out to twice the virial radius (Bryan & Norman 1998; Eke, Navarro, & Frenk 1998; Frenk et al. 1999). The bottom-left panel (c) of figure 13 shows the predicted  $C_l$  with the hot-gas extension cut out at 1, 2, or 3 times the virial radius. While a cut-off at the virial radius suppresses  $C_l$  at  $l < 5000$ , there is little difference for the cut-off at  $2r_{\text{vir}}$  and beyond. One should thus include the hot-gas extension beyond the virial radius; otherwise, one underestimates the power spectrum on large angular scales, but the actual position of the cut-off is not very important since the power spectrum converges at  $2r_{\text{vir}}$ .

The gas density profile in the inner region displays a core (Bryan & Norman 1998; Eke, Navarro, & Frenk 1998; Frenk et al. 1999), which is well reproduced by our model (Komatsu & Seljak 2001). On the other hand, recent X-ray observations have observed a decrease in temperature toward the centre within 5% of the virial radius (McNamara et al. 2000; Allen, Ettori, & Fabian 2001; Allen et al. 2001; Arnaud et al. 2001a; Arnaud et al. 2001b; Kaastra et al. 2001), which our polytropic model does not account for. The bottom-right panel (d) of figure 13 shows the predicted  $C_l$  with the inner region within 10%, 20%, or 40% of the virial radius excised. We find that the region interior to 10% of the virial radius has a negligible contribution to  $C_l$ , so the pressure profile in the cluster core has no effect on  $C_l$ . From this figure we find that the dominant contribution to  $C_l$  comes from around 20 – 40% of the virial radius, roughly corresponding to  $r_{2500}$ , which is just in the range of *Chandra* satellite for medium redshift clusters (McNamara et al. 2000; Allen, Ettori, & Fabian 2001; Allen et al. 2001) and well within *XMM/Newton* or *BeppoSax* (Arnaud et al. 2001a; Arnaud et al. 2001b; Kaastra et al. 2001). Recent observations confirm that the gas profile agrees well with the dark-matter profile in this region (Allen, Schmidt, & Fabian 2002), confirming our basic assumption. We note that the temperature gradient is still small over this range, so most of the pressure gradient is caused by the gas-density profile.

The effect of non-adiabatic physics has been investigated with hydrodynamic simulations. In da Silva et al. (2001b) it has been claimed that radiative cooling reduces  $C_l$  by modest amount, 20 – 40%, on all angular scales. This is presumably due to a decrease in the gas fraction, since some fraction of gas is being transformed into stars. Despite their extreme cooling treatment (giving too much cooled material to match the observations) the effect of radiative cooling is modest (note that 40% change in  $C_l$  gives a 5% change in  $\sigma_8$ ). Preheating may lead to a larger effect, as it may alter the gas structure not only in the inner region, but also at larger radii, especially for smaller-mass haloes. Some fraction of the gas may be expelled from the cluster, which would suppress the SZ fluctuations on small scales. At the same time, preheating increases the gas temperature, which would increase the spectrum. However, care must be taken not to violate the FIRAS constraints on the mean  $y$  parameter and it is unlikely that this could significantly enhance the SZ power spectrum without violating these limits. Several authors have noticed significant effects of preheating on  $C_l$  (Springel, White, & Hernquist 2001; Holder & Carlstrom 2001; da Silva et al. 2001b), although current treatments are still over-simplified. One must be careful in analytic models to make them self-consistent, as one cannot retain gas in hydrostatic equilibrium within external dark-matter potential using a large gas core and isothermal gas.

When hydrostatic equilibrium is imposed the pressure profile is less affected than the density or temperature profiles. It is likely that any preheating will have only a modest effect on the SZ power spectrum. Recently, White, Henquist, & Springel (2001) have used hydrodynamic simulations to show that gas cooling, energy feedback, and star formation affect  $C_l$  by no more than a factor of two, confirming our conclusion.

## 8 CONCLUSIONS

In this paper we present a refined analytic model for the angular power spectrum of the SZ effect. In contrast to previous modeling (Atrio-Barandela & Mücke 1999; Komatsu & Kitayama 1999; Cooray 2000; Molnar & Birkinshaw 2000; Holder & Carlstrom 2001; Zhang & Pen 2001), our model has no free parameters and treats the gas in a cluster dark-matter potential self-consistently, using the universal gas-density and temperature profile (Komatsu & Seljak 2001), which fits the observed and the simulated properties of clusters of galaxies in the range of interest to the SZ observations (outside 5% of the virial radius).

We compare our predictions for the spectrum and the errors with the hydrodynamic SZ simulations and find a good agreement. The deviations between our model and the simulations are comparable to the deviations among the simulations themselves and are particularly small in the observationally relevant range around  $l \sim 3000$ . Some of the discrepancies are due to either poor resolution in the simulations or sampling variance, while the remaining difference could be due to the simplifying assumptions of gas physics in our model, such as hydrostatic equilibrium, spherical symmetry, merging and substructure, which may be inaccurate in particular at higher redshifts when the clusters are still forming. The disagreement is more important on very small angular scales ( $l > 5000$ ), while the accuracy of our predictions in the range of  $l \sim 2000 - 5000$  is better than a factor of two, which translates to less than 10% systematic uncertainty in the amplitude of fluctuations  $\sigma_8$ . We also compare analytic predictions for the power-spectrum covariance matrix to the simulations and find similarly good agreement.

We investigate the dependence of  $C_l$  on various cosmological parameters, finding that over the range of interest  $\sigma_8$  and  $\Omega_b h$  determine the amplitude of  $C_l$  almost entirely, as has been pointed out by several authors before as well (Komatsu & Kitayama 1999; Seljak et al. 2001; Zhang & Pen 2001; Zhang et al. 2002). It is particularly important that the matter density of the universe does not affect the spectrum as much as  $\sigma_8$  does, in agreement with Komatsu & Kitayama (1999). This differs from the local-cluster-abundance studies, where the constraint is usually on  $\sigma_8 \Omega_m^{0.5}$ .

The dominant contribution to  $C_l$  comes from massive clusters ( $M > 10^{14} h^{-1} M_\odot$  for  $l < 5000$ ) at moderate ( $z \sim 1$ ) redshift. Within the cluster, the dominant contribution comes from around  $0.2 - 0.4 r_{\text{vir}}$ , suggesting that the physical processes taking place in the cluster core such as cooling, heating or heat conduction have little effect on the SZ power spectrum. We assume that the gas fraction is close to the cosmic mean baryon fraction, which is reasonable for massive clusters and has observational support in low stellar-mass-to-cluster-mass ratios in massive clusters (e.g., Fukugita, Hogan, & Peebles 1998), as well as in studies of the gas fraction as a function of radius (e.g., Allen, Schmidt, & Fabian 2002). While more exotic mechanisms such as preheating could affect  $C_l$  on all scales (by increasing the temperature and/or reducing the gas clumping), they are constrained by the FIRAS lim-

its and are unlikely to make more than a factor of two change in  $C_l$  (comparable to a 10% change in  $\sigma_8$ ).

Using analytic predictions for the spectrum and its covariance matrix we have performed a likelihood analysis to estimate how well we can measure  $\sigma_8$  against  $\Omega_m$  with realistic SZ observations. The likelihood is very sensitive to  $\sigma_8$  almost independent of  $\Omega_m$  (figure 9 or 10). By performing the likelihood analysis on the recently reported CBI (Mason et al. 2002) and BIMA (Dawson et al. 2002) detections at the level of  $15 - 20 \mu\text{K}$  at  $l \sim 2000 - 6000$  (figure 11), we find  $\sigma_8 (\Omega_b h / 0.035)^{2/7} = 1.04 \pm 0.12$  at the 95% statistical confidence level. To this we should add about 10% systematic theoretical uncertainty due to the simplified modeling in our model, the numerical issues in the simulations, and missing physics in both. We should note that most of the effects we have ignored within our model tend to further increase  $\sigma_8$ : assumed fiducial value for  $\Omega_b h = 0.035$  is somewhat high, we ignored fraction of gas transformed into stars, and our predictions are somewhat higher than the simulation results at the angular scales relevant for CBI and BIMA. These effects would further increase  $\sigma_8$ , although not by more than 5 - 10%. Such a high value for  $\sigma_8$  is in tension with the primary CMB amplitude determination (Lahav et al. 2002) and Ly- $\alpha$  forest determination (Croft et al. 1999; McDonald et al. 2000), although it can be accommodated by the cluster abundance and the weak lensing results if  $\Omega_m \sim 0.2 \pm 0.1$ . While the CBI experiment is surveying  $1 \text{ deg}^2$  of the sky and still has a large instrumental noise, a somewhat larger sky coverage with lower noise (e.g., SZA) would significantly reduce the statistical errors on  $\sigma_8$ . Surveys with  $100 \text{ deg}^2$  such as ACT or AMIBA should be able to measure both the power spectrum and its covariance matrix (e.g. by using bootstrap sampling) to exquisite precision.

In conclusion, measurement of the angular power spectrum of the SZ effect offers a promising way to determine  $\sigma_8$ , since it is very sensitive to its value and is almost independent of  $\Omega_m$ . It is free of observational selection effects such as flux, surface brightness, or volume limit of the survey. It does not require the mass of sampled haloes to be measured, and there is no uncertainty associated with the mass-flux calibration. Finally, it is within reach of the next generation of small-scale CMB experiments and may have already been detected by the CBI and BIMA experiments, in which case their results imply that the amplitude of fluctuations at  $8 h^{-1} \text{ Mpc}$  scale is of order unity.

## ACKNOWLEDGMENTS

We would like to thank Antonio C. da Silva, Alexandre Refregier, Volker Springel, Pengjie Zhang, and their collaborators for providing us with their hydrodynamic simulation data results. We would like to thank John E. Carlstrom, Carlo Contaldi, Gilbert P. Holder, Wayne Hu, Andrey V. Kravtsov, Ue-Li Pen, Masahiro Takada, and Pengjie Zhang for discussions. U. S. acknowledges the support of NASA and Packard and Sloan Foundation Fellowships.

## REFERENCES

- Allen S. W., Ettori S., Fabian A. C., 2001, MNRAS, 324, 877
- Allen S. W., Schmidt R. W., Fabian A. C., 2001, MNRAS, 328, L37
- Allen S. W., Schmidt R. W., Fabian A. C., 2002, MNRAS, in press (astro-ph/0205007)
- Allen S. W. et al., 2001, MNRAS, 324, 842
- Arnaud M. et al., 2001a, A&A, 365, L67

- Arnaud M., Neumann D. M., Aghanim N., Gastaud R., Majerowicz S., Hughes J. P., 2001b, *A&A*, 365, L80
- Atrio-Barandela F., Mücke J. P., 1999, *ApJ*, 515, 465
- Bahcall N. A., Fan X., 1998, *ApJ*, 504, 1
- Bardeen J. M., Bond J. R., Kaiser N., Szalay A. S., 1986, *ApJ*, 304, 15
- Bean R., Melchiorri A., 2002, *Phys. Rev. D*, 65, 41302
- Birkinshaw M., 1999, *Phys. Rep.*, 310, 97
- Bond J. R. et al., 2002, *ApJ*, submitted (astro-ph/0205386)
- Bryan G. L., Norman M. L., 1998, *ApJ*, 495, 80
- Bullock J. S., Kolatt T. S., Sigad Y., Somerville R. S., Kravtsov A. V., Klypin A. A., Primack J. R., Dekel A., 2001, *MNRAS*, 321, 559
- Church S. E., Ganga K. M., Ade P. A. R., Holzzapfel W. L., Mauskopf P. D., Wilbanks T. M., Lange A. E., 1997, *ApJ*, 484, 523
- Cole S., Kaiser N., 1988, *MNRAS*, 233, 637
- Cooray A., 2000, *Phys. Rev. D*, 62, 103506
- Cooray A., 2001, *Phys. Rev. D*, 64, 63514
- Cooray A., Hu W., Miralda-Escudé J., 2000, *ApJ*, 535, L9
- Croft R. A. C., Weinberg D. H., Pettini M., Hernquist L., Katz N., 1999, *ApJ*, 520, 1
- da Silva A. C., Barbosa D., Liddle A. R., Thomas P. A., 2000, *MNRAS*, 317, 37
- da Silva A. C., Barbosa D., Liddle A. R., Thomas P. A., 2001a, *MNRAS*, 326, 155
- da Silva A. C., Kay S. T., Liddle A. R., Thomas P. A., Pearce F. R., Barbosa D., 2001b, *ApJ*, 561, L15
- Dawson K. S., Holzzapfel W. L., Carlstrom J. E., Joy M., LaRoque S. J., Reese E. D., 2001, *ApJ*, 553, L1
- Dawson K. S., Holzzapfel W. L., Carlstrom J. E., LaRoque S. J., Miller A., Nagai D., Joy M., 2002, *ApJ*, submitted (astro-ph/0206012)
- Eke V. R., Cole S., Frenk C. S., 1996, *MNRAS*, 282, 263
- Eke V. R., Navarro J. F., Frenk C. S., 1998, *ApJ*, 503, 569
- Eke V. R., Navarro J. F., Steinmetz M., 2001, *ApJ*, 554, 114
- Evrard A. E. et al., 2002, *ApJ*, 573, 7
- Frenk C. S. et al., 1999, *ApJ*, 525, 554
- Fukugita M., Hogan C. J., Peebles P. J. E., 1998, *ApJ*, 503, 518
- Ganga K., Ratra B., Church S. E., Sugiyama N., Ade P. A. R., Holzzapfel W. L., Mauskopf P. D., Lange A. E., 1997, *ApJ*, 484, 517
- Haiman Z., Mohr J. J., Holder G. P., 2001, *ApJ*, 553, 545
- Holder G. P., Carlstrom J. E., 2001, *ApJ*, 558, 515
- Holzzapfel W. L., Carlstrom J. E., Grego L., Holder G., Joy M., Reese E. D., 2000, *ApJ*, 539, 57
- Hu W., 2001, *Phys. Rev. D*, 64, 83005
- Hu W., Kravtsov A. V., 2002, *ApJ*, submitted (astro-ph/0203169)
- Jenkins A., Frenk C. S., White S. D. M., Colberg J. M., Cole S., Evrard A. E., Couchman H. M. P., Yoshida N., 2001, *MNRAS*, 321, 372
- Jing Y. P., Suto Y., 2000, *ApJ*, 529, L69
- Kaastra J. S., Ferrigno C., Tamura T., Paerels F. B. S., Peterson J. R., Mittaz J. P. D., 2001, *A&A*, 365, L99
- Kitayama T., Suto Y., 1997, *ApJ*, 490, 557
- Klypin A., Kravtsov A. V., Bullock J. S., Primack J. R., 2001, *ApJ*, 554, 903
- Komatsu E., Kitayama T., 1999, *ApJ*, 526, L1
- Komatsu E., Seljak U., 2001, *MNRAS*, 327, 1353
- Lacey C., Cole S., 1993, *MNRAS*, 262, 627
- Lahav O. et al., 2002, *MNRAS*, 333, 961
- Makino N., Sasaki S., Suto Y., 1998, *ApJ*, 497, 555
- Makino N., Suto Y., 1993, *ApJ*, 405, 1
- Mason B. S. et al., 2002, *ApJ*, submitted (astro-ph/0205384)
- McDonald P., Miralda-Escudé J., Rauch M., Sargent W. L. W., Barlow T. A., Cen R., Ostriker J. P., 2000, *ApJ*, 543, 1
- McNamara B. R. et al., 2000, *ApJ*, 534, L135
- Molnar S. M., Birkinshaw M., 2000, *ApJ*, 537, 542
- Moore B., Governato F., Quinn T., Stadel J., Lake G., 1998, *ApJ*, 499, L5
- Nakamura T. T., Suto Y., 1997, *Progress of Theoretical Physics*, 97, 49
- Navarro J. F., Frenk C. S., White S. D. M., 1997, *ApJ*, 490, 493
- Padin S. et al., 2001, *ApJ*, 549, L1
- Partridge R. B., Richards E. A., Fomalont E. B., Kellermann K. I., Windhorst R. A., 1997, *ApJ*, 483, 38
- Pearce F. R., Couchman H. M. P., 1997, *New Astronomy*, 2, 411
- Pen U., 1998, *ApJS*, 115, 19
- Persi F. M., Spergel D. N., Cen R., Ostriker J. P., 1995, *ApJ*, 442, 1
- Pierpaoli E., Scott D., White M., 2001, *MNRAS*, 325, 77
- Press W. H., Schechter P., 1974, *ApJ*, 187, 425
- Refregier A., Komatsu E., Spergel D. N., Pen U., 2000, *Phys. Rev. D*, 61, 123001
- Refregier A., Teyssier R., 2000, *PRD*, submitted (astro-ph/0111285)
- Scaramella R., Cen R., Ostriker J. P., 1993, *ApJ*, 416, 399
- Seljak U., 2000, *MNRAS*, 318, 203
- Seljak U., 2001, *MNRAS*, submitted (astro-ph/0111362)
- Seljak U., Burwell J., Pen U., 2001, *Phys. Rev. D*, 63, 619
- Springel V., White M., Hernquist L., 2001, *ApJ*, 549, 681
- Springel V., Yoshida N., White S. D. M., 2001, *New Astronomy*, 6, 79
- Subrahmanyan R., Kesteven M. J., Ekers R. D., Sinclair M., Silk J., 1998, *MNRAS*, 298, 1189
- Sugiyama N., 1995, *ApJS*, 100, 281
- Sunyaev R. A., Zeldovich I. B., 1980, *ARA&A*, 18, 537
- Teyssier R., 2002, *A&A*, 385, 337
- Van Waerbeke L., Mellier Y., Pello R., Pen U.-L., McCracken H. J., Jain B., 2002, *A&A*, submitted (astro-ph/0202503)
- Viana P. T. P., Liddle A. R., 1996, *MNRAS*, 281, 323
- Viana P. T. P., Nichol R. C., Liddle A. R., 2002, *ApJ*, 569, L75
- White M., 2001, *A&A*, 367, 27
- White M., Henquist L., Springel V., 2001, *ApJ*, submitted (astro-ph/0107023)
- White S. D. M., Efstathiou G., Frenk C. S., 1993, *MNRAS*, 262, 1023
- Zhang P., Pen U., 2001, *ApJ*, 549, 18
- Zhang P., Pen U., Wang B., 2002, *ApJ*, submitted (astro-ph/0201375)

**Table 1.** Simulation parameters. The first column assigns a label to each simulation. The second column shows the name of a code which each simulation uses: MMH (=Moving-Mesh Hydrodynamic code) (Pen 1998), and RAMSES (adaptive mesh-refinement hydrodynamic code) (Teyssier 2002) are mesh codes, while GADGET (=GALaxies with Dark matter and Gas intEracT code) (Springel, Yoshida, & White 2001), and HYDRA (Pearce & Couchman 1997) are SPH (=Smoothed-Particle Hydrodynamic) codes. The third column shows the number of grids for mesh codes (MMH and RAMSES), or the number of SPH particles for SPH codes (GADGET and HYDRA). The box size of simulations is  $100 h^{-1}$  Mpc except for SWH01, which uses  $134 h^{-1}$  Mpc. The fourth column shows the number of two-dimensional maps which each simulation has created. The fifth column shows the field-of-view of the simulated two-dimensional maps. Note that RKSP00 and RT00 have not created two-dimensional maps, but computed the SZ angular power spectrum from the three-dimensional SZ power spectrum. The sixth–eighth columns show the cosmological parameters which each simulation uses. All the simulations use  $\Omega_\Lambda = 1 - \Omega_m$ , and  $n = 1.0$ . The rightmost column shows references for the simulations.

Label	Code	$N_{\text{grid}}$ or $N_{\text{sph}}$	$N_{\text{map}}$	F.O.V.	$\Omega_m$	$\Omega_b$	$h$	$\sigma_8$	Reference
RKSP00	MMH	$128^3$	—	—	0.37	0.049	0.7	0.8	Refregier et al. (2000)
SBP01	MMH	$256^3$	12	$2^\circ \times 2^\circ$	0.37	0.049	0.7	0.8	Seljak, Burwell, & Pen (2001)
SWH01	GADGET	$224^3$	15	$1^\circ \times 1^\circ$	0.3	0.04	0.67	0.9	Springel, White, & Hernquist (2001)
daSilva01	HYDRA	$160^3$	30	$1^\circ \times 1^\circ$	0.35	0.0377	0.71	0.9	da Silva et al. (2001b)
RT00	RAMSES	$256^3$	—	—	0.3	0.039	0.7	0.93	Refregier & Teyssier (2000)
ZPW02	MMH	$512^3$	40	$1^\circ 19' \times 1^\circ 19'$	0.37	0.05	0.7	1.0	Zhang, Pen, & Wang (2002)

## APPENDIX A: GAS POLYTROPIC INDEX

In this appendix we derive an exact formula for the gas polytropic index  $\gamma$  and give fitting formulae for  $\gamma$  and for the mass–central temperature normalization factor,  $\eta(0)$  (equation 19).

We specify  $\gamma$  and  $\eta(0)$  uniquely by requiring that the gas-density profile,  $\rho_{\text{gas}}(x)$ , matches the dark-matter density profile,  $\rho_{\text{dm}}(x)$ , in outer parts of the haloes. We do this by solving the following equation,

$$s_* \equiv \left. \frac{d \ln \rho_{\text{gas}}(x)}{d \ln x} \right|_{x=x_*} = \left. \frac{d \ln \rho_{\text{dm}}(x)}{d \ln x} \right|_{x=x_*}, \quad (\text{A1})$$

where  $s_*$  denotes a slope of the dark-matter density profile at a matching radius  $x_*$ .

In previous paper (Komatsu & Seljak 2001) we have shown that equation (A1) determines  $\eta(0)$  uniquely for a given  $\gamma$ ,

$$\eta(0) = \gamma^{-1} \left\{ \left( \frac{-3}{s_*} \right) \left[ \frac{x_*^{-1} m(x_*)}{c^{-1} m(c)} \right] + 3(\gamma - 1) \left[ \frac{c}{m(c)} \right] \int_0^{x_*} du \frac{m(u)}{u^2} \right\}, \quad (\text{A2})$$

where  $m(x)$  is a non-dimensional dark-matter mass profile defined by

$$m(x) \equiv \rho_s^{-1} \int_0^x du u^2 \rho_{\text{dm}}(u), \quad (\text{A3})$$

and  $\rho_s$  is a scale density. Equation (A2) makes the matching condition, equation (A1), satisfied at radius  $x_*$ .

Next, we require that  $\eta(0)$  does not depend upon a particular choice of  $x_*$ ; this requirement specifies  $\gamma$  uniquely. While we have done this by finding an empirical fitting formula for  $\gamma$  in the previous paper (equation 25 of Komatsu & Seljak 2001), we derive here an exact formula for  $\gamma$  by solving the following equation,

$$\left. \frac{\partial \eta(0)}{\partial x_*} \right|_{x_*=c} = 0, \quad (\text{A4})$$

where  $c$  is the concentration parameter (see equation 10 for definition). This equation means that  $\eta(0)$  normalization does not depend upon the particular choice of  $x_*$ .

We find that equation (A4) gives  $\gamma$  as a function of  $c$ ,

$$\gamma = 1 - \frac{1}{s_*} \left. \frac{\partial \ln [m(x_*)/s_*]}{\partial \ln x_*} \right|_{x_*=c}. \quad (\text{A5})$$

This formula gives the polytropic index of gas in haloes with any given dark-matter density profiles.

Hereafter, we evaluate  $\gamma$  and  $\eta(0)$  for the NFW profile (Navarro, Frenk, & White 1997),  $\rho_{\text{dm}}(x) = \rho_s x^{-1} (1+x)^{-2}$ . We find

$$s_* = -\frac{1+3x_*}{1+x_*}, \quad (\text{A6})$$

and

$$m(x) = \ln(1+x) - \frac{x}{1+x}. \quad (\text{A7})$$

By substituting  $s_*$  and  $m(x)$  into equation (A5), we obtain  $\gamma$ . We then substitute  $s_*$ ,  $m(x)$ , and the derived  $\gamma$  into (A2) to obtain  $\eta(0)$ .

The upper panel of figure A1 shows  $\gamma$  as a function of  $c$  compared to the fitting formula in equation (17). For comparison, the figure also plots the fitting formula which we have given for  $4 < c < 11$  in Komatsu & Seljak (2001). The new formula, equation (17), is valid for  $1 < c < 25$ .

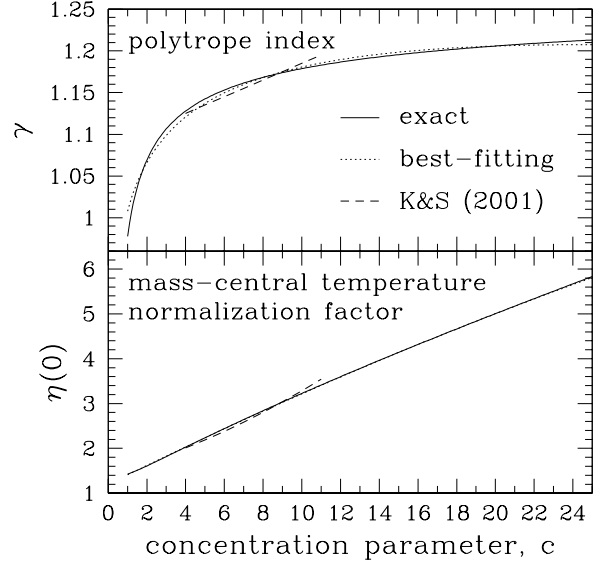


**Figure A1.** The top panel shows the polytropic index of gas in haloes,  $\gamma$ , while the bottom panel shows the mass–central temperature normalization factor,  $\eta(0)$  (equation 19), as a function of the concentration parameter  $c$ . The solid lines plot exact values calculated from equation (A5) and (A2) for  $\gamma$  and  $\eta(0)$ , respectively. The dotted lines plot the best-fitting formulae, equation (17) and (18) for  $\gamma$  and  $\eta(0)$ , respectively. The dashed lines plot the fitting formulae given in Komatsu & Seljak (2001) for  $4 < c < 11$ .

By substituting  $\gamma$  from equation (A5) into equation (A2) we obtain  $\eta(0)$  as a function of  $c$ . The bottom panel of figure A1 shows  $\eta(0)$  as a function of  $c$  and also the fitting formula  $\eta(0)$  in equation (18). For comparison, the figure also plots the fitting formula given in Komatsu & Seljak (2001).